Injection of a viscoplastic material inside a tube or between two parallel disks: Conditions for wall detachment of the advancing front

John Papaioannou, George Karapetsas, Yannis Dimakopoulos,[a] and John Tsamopoulos[b]

Department of Chemical Engineering, Laboratory of Computational Fluid Dynamics, University of Patras, Patras 26500, Greece

(Received 28 January 2009; final revision received 25 June 2009)

Synopsis

The injection of a viscoplastic material, driven by a constant pressure drop, inside a pipe or between two parallel coaxial disks under creeping flow conditions is examined. The transient nature of both flow arrangements requires solving a time-dependent problem and fully accounting for the advancing liquid/air interface. Material viscoplasticity is described by the Papanastasiou constitutive equation. A quasi-elliptic grid generation scheme is employed for the construction of the mesh, combined with local mesh refinement near the material front and, periodically, full mesh reconstruction. All equations are solved using the mixed finite element/Galerkin formulation coupled with the implicit Euler method. For a viscoplastic fluid, the flow field changes qualitatively from that of a Newtonian fluid because the material gets detached from the walls. For small Bingham numbers, the contact line moves in the flow direction, so that initially the flow resembles that of a Newtonian fluid, but even in that case detachment eventually occurs. The distance covered by the contact line, before detachment takes place, decreases as the Bingham number increases. For large enough Bingham numbers, the fluid may even detach from the wall without advancing appreciably. In pipe flow, when detachment occurs, unyielded material arises at the front and the flow changes into one under constant flow rate with pressure distribution that does not vary with time. In the flow between disks, it remains decelerating and the material keeps rearranging at its front because of the increased cross section through which it advances. The wall detachment we predict has been observed experimentally by Bates and Bridgwater [Chem. Eng. Sci. **55**, 3003–3012 (2000)] in radial flow of pastes between two disks. © *2009 The Society of Rheology.* [DOI: 10.1122/1.3191779]

I. INTRODUCTION

The transient injection of a viscoplastic fluid inside a pipe or between two parallel disks is examined. Both of these flows are encountered in several processes with practical interest. For example, the radial flow between two parallel disks is a model of the process of filling with cement thin fractures at the walls of oil wells in the oil industry, in order to avoid oil leakage into them and deterioration of the well operation [Peysson *et al.*

[a]Present address: Department of Biomedical Engineering, Eindhoven University of Technology, P.O. Box 513, 5600 MB, The Netherlands; electronic mail: dimako@chemeng.upatras.gr

[b]Author to whom correspondence should be addressed; FAX: +(30) 2610-996-178; electronic mail: tsamo@chemeng.upatras.gr

(2005); Peysson (private communication, 2006)]. A similar application but in a larger scale is that of grout injection in large cavities created in underground mines. This filling of the gaps that separate the successive layers of rocks with coal mine and power plant waste materials is essential to avoid mine subsidence [Mills (2001)]. In addition, various industrial processes include radial flow of pastes between flat surfaces, for example, in ceramic manufacturing [Huang and Oliver (1999)]. Pipe flow of a viscoplastic material is encountered in various engineering processes. Some of them are the transport of waxy crude oil through pipelines [Vinay *et al.* (2006)], of lignite-in-water slurries for the exploitation of lignite deposits [Davis and Mai (1991)], and the pumping of mud suspensions during the drilling of a borehole [Billingham and Ferguson (1993)]. Our aim here is to develop rigorous and efficient predictive tools capable of simulating both flows of viscoplastic materials.

The materials mentioned above are all viscoplastic: they do not obey Newton's law of viscosity, but a constitutive law that distinguishes two different material behaviors in their volume. In the first one, the material behaves as a viscous inelastic liquid and, therefore, it flows with a viscosity that depends on the local rate of strain, while in the other one it behaves as a rigid solid. The first constitutive law proposed to describe this material behavior is the Bingham model [Bingham (1922)]. It states that in the first region the second invariant of the stress $\|\underline{\underline{\tau}}^*\|$ exceeds a particular value, which is called yield stress, and the material viscosity is finite and constant, whereas in the second one, $\|\underline{\underline{\tau}}^*\|$ is equal to or less than this value and the viscosity is practically infinite. Early on, this model was applied only in one-dimensional (1D) flows. In the context of radial flow between disks, Dai and Bird (1981) used it first to obtain an analytical solution for the flow in a plane slit and then tried to extend this solution to radial flow. In this way, they predicted an unyielded region around the plane of symmetry between the disks. Unfortunately, this is known to be false, as explained by Lipscomb and Denn (1984) and by Smyrnaios and Tsamopoulos (2001). As the common boundary of the two distinct regions (the so-called yield surface) is approached, the exact Bingham model becomes singular. The complexity in applying this model increases because the yield surface is usually not known *a priori* but must be determined as part of the solution. In simple flows, for which analytical solutions are possible, this singularity does not generate a problem, but, in more complex flows which require numerical solution, it leads to profound computational problems. A rare successful analysis of a two-dimensional (2D) flow, where this constitutive law was used, was presented by Beris *et al.* (1985), who computed the creeping flow around a falling isolated sphere in a viscoplastic fluid. Even in this very basic flow, a complicated numerical solution was needed to find the shape and location of the yield surfaces. Another exception is the case of Vinay *et al.* (2006), who examined the start up of weakly compressible pipeline flows of waxy crude oils. It required a complex method based on Lagrange multipliers to solve numerically the system of equations including the aforementioned constitutive law. The same method was used by Roquet and Saramito (2003) to determine the flow of viscoplastic fluids around a cylinder. Finally, approximate solutions can be obtained by applying variational principles, e.g., Frigaard *et al.* (2003) and Dubash and Frigaard (2004).

In order to overcome such difficulties, several modifications of the Bingham constitutive equation have been introduced to produce a non-singular constitutive law, by introducing some "regularization" parameter [Frigaard and Nouar (2005)]. Besides, experiments have not shown definitively that such a singularity actually exists [Barnes (1999)]. In the present study, we will use one such model, which seems to perform better than the others according to Frigaard and Nouar (2005), the exponential model proposed by Papanastasiou (1987),

$$\underline{\underline{\tau}}^* = -\left[\mu_o^* + \frac{\tau_y^*(1-e^{-m^*\dot{\gamma}^*})}{\dot{\gamma}^*}\right]\underline{\underline{\dot{\gamma}}}^*, \tag{1}$$

where $\underline{\underline{\dot{\gamma}}}^*$ is the rate of strain tensor, defined as $\underline{\underline{\dot{\gamma}}}^* = \nabla^* \underline{v}^* + (\nabla^* \underline{v}^*)^T$, $\dot{\gamma}^*$ is its second invariant, $\dot{\gamma}^* = \left[\frac{1}{2}\underline{\underline{\dot{\gamma}}}^* : \underline{\underline{\dot{\gamma}}}^*\right]^{1/2}$, and m^* is the stress growth exponent or regularization parameter. The symbols that are followed by an asterisk denote dimensional quantities, and this convention will be used hereafter. In the limit that $m^* \to \infty$, the original Bingham model is recovered. In fact the predictions of these two models are indistinguishable in the quasi-steady squeeze flow studied by Smyrnaios and Tsamopoulos (2001), when large enough values of m^* are used. However, Burgos *et al.* (1999) argued that too large values should not be used because they adversely affect the numerical stability and stiffness of the resulting discrete system. The Papanastasiou model has been extensively used by several researchers in the past. For example, Matsoukas and Mitsoulis (2003) and Florides *et al.* (2007) used it to study the quasi-steady squeeze flow and Tsamopoulos *et al.* (2008) used it to determine the flow around a rising and deformable bubble. In transient flows, Tsamopoulos *et al.* (1996) employed it to simulate the thinning of a viscoplastic fluid film on a rotating disk in the process of spin coating, Dimakopoulos and Tsamopoulos (2003a) used it to study the displacement of a viscoplastic material by air in straight and suddenly constricted tubes, Karapetsas and Tsamopoulos (2006) used it to study the transient squeeze flow of viscoplastic materials under either a constant disk velocity or a constant applied force on the disks, and Chatzimina *et al.* (2007) used it to examine the cessation of annular Poiseuille flow, where they calculated the time for the complete cessation of this flow.

The key feature of the flows examined herein is their transient character, which is partly due to the moving and deforming interfaces. The first who described the behavior of an advancing liquid front in a duct was Rose (1961). He used the terms "fountain effect" and "spill over," to describe the motion of fluid elements as they decelerated while approaching the interface, if that motion is observed with a reference frame moving with the interface, and moved toward the wall. Several contributions on fountain flow have been reported since then. As such, we mention the work of Mavridis *et al.* (1986), who simulated the transient flow of a highly viscous Newtonian fluid between two flat infinite plates. They found that the fluid elements behind the advancing flow front eventually take a V-shape, in complete agreement with experiments. Actually, Coyle *et al.* (1987) completed this picture and showed that the complex shear and elongational deformation histories of fluid particles in fountain flow lead to a "mushroom" shape of a tracer line initially placed perpendicular to the axis of symmetry and away from the flow front. Behrens *et al.* (1987) carried out experiments with Newtonian fluids advancing in a cylindrical tube and presented numerical simulations. Mavridis *et al.* (1988) simulated the flow of a Newtonian fluid inside a tube, using the results of Behrens *et al.* (1987) for validation. Fountain flow has also been studied with various, more complex fluids. Quite recently, Grillet *et al.* (2002) conducted both experimental and numerical work in analyzing surface defects, which arise in injection molding of polymer melts. They concluded from the experiments that these defects are caused by flow instabilities during the filling of the mold, while the stability analysis that they performed predicted accurately these instabilities. Later on, Bogaerds *et al.* (2004) extended this work by investigating the effect of fluid elasticity on the stability characteristics of the injection molding process.

Radial flow between parallel disks has also been extensively studied in the literature. Some notable contributions are those of Berger and Gogos (1973) and Wu *et al.* (1974),

who simulated numerically the transient non-isothermal flow of power-law fluids, and of Co and Stewart (1982), who provided the numerical solution for the steady isothermal viscoelastic flow from a tube into a radial slit. More recently, Chung and Kwon (2002) solved for the non-isothermal Stokes flow of fiber suspensions in center-gated disks and in a film-gated strip predicting, additionally, fiber orientation. On the other hand, experimental work associated with the injection flow between parallel disks was reported by Bates and Bridgwater (2000), who used pastes for their experiments and provided useful observations, while Peysson *et al.* (2005) and Peysson (private communication, 2006) carried out experiments and approximate analysis with a Newtonian fluid and bentonite mud.

The two primary ways by which injection of a fluid inside a cylindrical tube or between two parallel disks can take place are either under a constant flow rate or under a constant pressure drop applied between the inlet and the outlet, depending on the application. In the present work, we studied the case in which the flow is generated by a constant pressure drop. We perform transient simulations of both flows and study the effect of the yield stress on the velocity and pressure fields, as well as on the location and shape of the advancing front and the yield surfaces. Moreover, we highlight the qualitative departure of the flow field in such materials from that of Newtonian fluids as their yield stress increases.

The governing equations and the boundary conditions for both problems are given in Sec. II. The finite element algorithm as well as mesh generation and refinement techniques are described in Sec. III. In Sec. IV we present the results of the complete parametric analysis of both flows. Finally, conclusions are drawn in Sec. V.

II. PROBLEM FORMULATION

We consider the isothermal flow of a viscoplastic fluid with a constant yield stress τ_y^* and, upon yielding, a constant dynamic viscosity μ_o^*. We assume that the fluid is incompressible with a constant density ρ^* and that the fluid-air interface has a constant interfacial tension σ^*. This work deals with two different flow geometries, which, however, share many common elements as we will see below. In the first one, presented schematically in Fig. 1(a), a pipe of inner radius R^* is partially filled with a viscoplastic fluid. The initial control volume of the fluid is a perfect cylinder of radius R^* and length equal to the axial distance between the location, where a constant pressure is applied and the initially flat liquid front L^*. The second geometry is shown schematically in Fig. 1(b). Here, the material is injected through a hole in the center of two parallel and co-axial disks to fill the space between them. Initially, this space is partially filled with material, while the free surface of the fluid is a perfectly cylindrical one. To eliminate the effect of the flow rearrangement that takes place near the injection hole, we define the initial control volume so that its inflow boundary at L_1^* and the initial position of the liquid/air interface are far enough from it. Their actual values are determined numerically by trial and error. This procedure makes again the flow field at the inflow boundary nearly 1D. The short-dotted lines in Fig. 1(b) indicate the initial control volume. Moreover, to make sure that the pressures on the inflow boundary do not undergo appreciable variation during the flow, the initial distance of the free surface from it, L^* and L_2^*, is large enough, so that a sufficient amount of fluid exists at start up in the control volume. These simplifications permit us to avoid additional computational cost without losing any of the significant characteristics of the flows examined in this paper. Moreover, assuming that gravitational forces are negligible, which is often the case for such flows of viscoplastic materials [see, for example, Karapetsas and Tsamopoulos (2006)], we can introduce additional symme-

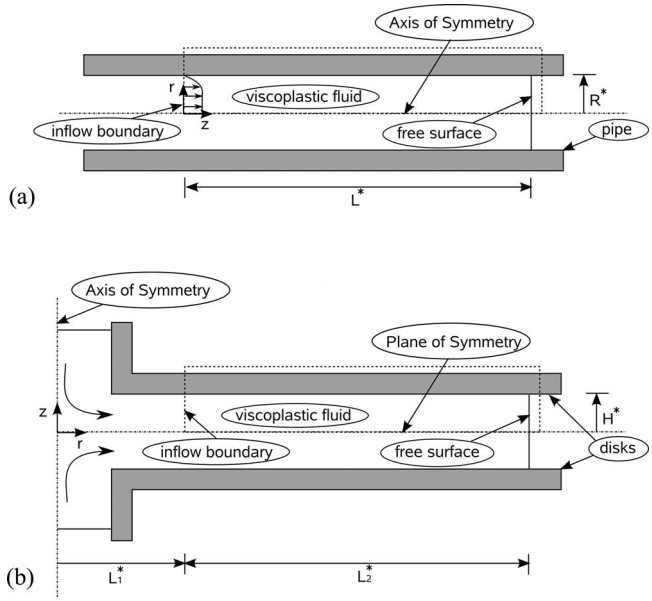

FIG. 1. Initial arrangement of a finite amount of viscoplastic fluid (a) in a semi-infinite pipe and (b) between parallel and coaxial disks.

tries in the flow: an axis of symmetry at $r^*=0$ in the case of pipe flow or a plane of symmetry at $z^*=0$ in the case of radial flow. In both cases, the pressure inside the fluid is uniform initially, while the ambient pressure is taken to be zero. At start up, the pressure of the air remains zero, whereas the pressure of the fluid at the inflow boundary is increased abruptly from zero to P^*_{in}, thus, setting the fluid in motion. This change causes fluid injection in both geometries and deformation of the liquid/air interface.

For scaling the governing equations, we choose as characteristic length for the pipe flow its radius R^* and for the radial flow the half distance between the two disks H^*. Time is scaled with D^*/V^*, where D^* stands for either H^* or R^* in the corresponding problem, and V^* is a characteristic velocity. Pressure and stresses are scaled with the viscous scale $\mu_0^* V^*/D^*$. There are at least two choices for the characteristic velocity:

(a) Because of the monotonically decelerating nature of both flows, one may select as V^* the velocity at the intersection of the fluid/air interface with the plane or the axis of symmetry, depending on the geometry, at $t=0^+$. This choice is convenient because it sets its maximum dimensionless value to unity always, irrespective of the fluid yield stress, the applied pressure, or the initial amount of fluid. This ensures that the order of magnitude of $\dot{\gamma}$ is large enough, allowing us to use the same moderate values for the dimensionless exponent $N=m^*V^*/D^*$ in the Papanastasiou constitutive equation and achieve convergence to the original Bingham model, even when $\dot{\gamma}$ is reduced by about one order of magnitude toward the end of the simulations. The validity of our choice for the dimensionless exponent $N\sim 300-400$ has been confirmed by numerous numerical experiments. In other words, we have made a consistent choice of this regularizing parameter as recommended by the analysis of Frigaard and Nouar (2005). Moreover, the same strict criterion 10^{-10} for convergence of the Newton–Raphson iterations can be used. Then, the dimensionless groups that arise are the Reynolds number $\text{Re}=\rho^* V^* D^*/\mu_0^*$, the

Bingham number $\mathrm{Bn}=\tau_y^*D^*/\mu_0^*V^*$, and the Capillary number $\mathrm{Ca}=\mu_0^*V^*/\sigma^*$. In addition, the geometric ratios that arise are $l=L^*/R^*$ for the pipe flow and $l_1=L_1^*/H^*$ and $l_2=L_2^*/H^*$ for the radial flow between the disks.

(b) Alternatively, the scaling can be based on the applied pressure difference ΔP^*, and V^* can be derived from it ignoring the flow in the advancing front (in the case of the pipe, this is like assuming fully developed Stokes flow) and balancing the pressure difference driving the flow ΔP^* to the wall shear stress $\mu_0^*V^*/D^*$, yielding $V^*=\Delta P^*D^*/\mu_0^*$. Then the dimensionless variables and groups will be defined differently and will be indicated by an overbar. Their values are related to those defined above as follows:

$$\overline{\Delta P}=1,\ \ \bar{V}=V/P_{\mathrm{in}},\ \ \bar{t}=P_{\mathrm{in}}/t,\ \ \overline{\mathrm{Bn}}\equiv\tau_y^*/\Delta P^*=\mathrm{Bn}/P_{\mathrm{in}},\ \text{ and }\ \bar{N}\equiv m^*\Delta P^*/\mu_0^*=m^*V^*/D^*$$
$$=NP_{\mathrm{in}}, \tag{2}$$

where P_{in} is the initial dimensionless pressure difference according to the first scaling (a) and determined by our simulations, and N is the dimensionless exponent in the Papanastasiou model. For the reasons presented in (a), we have used the first scaling in the simulations and the results to be presented subsequently. The last relation in Eq. (2) is especially important. It indicates that the dimensionless exponent according to scaling (b) should increase with the applied pressure, whereas according to scaling (a) it can be kept constant. Moreover, the numerical values required for $\bar{N}$ should be 30–60 times larger (depending on P_{in} which in turn depends on the other problem parameters) than our N values in order for the Papanastasiou model to be close enough to the original Bingham model. This is another indication that, although the values we used for the dimensionless exponent may seem low, they correspond to much higher values of the exponent one would have to use with the scalings in (b).

The flow of an incompressible fluid is governed by the momentum and mass conservation equations, which, in their dimensionless form, are

$$\mathrm{Re}\frac{D\underline{v}}{Dt}+\underline{\nabla}P+\underline{\nabla}\cdot\underline{\underline{\tau}}=0, \tag{3}$$

$$\underline{\nabla}\cdot\underline{v}=0, \tag{4}$$

where $\underline{\underline{\tau}}$ is the viscous part of the total stress tensor $\underline{\underline{\sigma}}$,

$$\underline{\underline{\sigma}}=-P\underline{\underline{I}}+\underline{\underline{\tau}}, \tag{5}$$

$\underline{v}$, P are the axisymmetric velocity vector and the pressure, respectively, while D/Dt denotes the material derivative and ∇ denotes the gradient operator. Under typical experimental conditions for viscoplastic materials, creeping flow conditions prevail and hereafter we will take $\mathrm{Re}=0$. To complete the description of the flow problem, a constitutive equation that describes the rheology of the fluid is required. In the present study, we employ the regularized constitutive model proposed by Papanastasiou (1987), which relates the stress tensor $\underline{\underline{\tau}}$ to the rate of strain tensor $\dot{\underline{\underline{\gamma}}}$ by a simple relation with exponential dependence of the effective viscosity on the rate of strain. The dimensionless form of this constitutive equation is

$$\underline{\underline{\tau}}=-\left[1+\mathrm{Bn}\frac{1-e^{-N\dot{\gamma}}}{\dot{\gamma}}\right]\dot{\underline{\underline{\gamma}}}, \tag{6}$$

where N is the stress growth exponent $N=m^*V^*/D^*$. In the simulations to be presented in this paper, we have chosen $N=400$ for the radial flow problem, so that this parameter

does not affect our predictions. The same value was used for the pipe flow for $\mathrm{Bn} \leq 2$. However, for this geometry we found that for higher values of Bn, it was necessary to lower this value to 300 because convergence could not be easily obtained with higher values of N and still results were not affected by this lower choice.

A. Boundary and initial conditions

The boundary conditions will be presented for conciseness in a general formulation for both problems. Hereafter, we will indicate with $\underline{n}$ and $\underline{t}$ the outward unit normal and unit tangential vectors, respectively, on the corresponding boundary. Along the free surface, the velocity field should satisfy a local force balance between surface tension and viscous stresses in the liquid, setting the pressure in the surrounding gas to zero (datum pressure)

$$\underline{n} \cdot \underline{\underline{\sigma}} = \frac{2H}{\mathrm{Ca}} \underline{n}, \tag{7}$$

where $2H$ is the mean curvature of the free surface, defined as

$$2H = -\underline{\nabla}_s \cdot \underline{n}, \quad \underline{\nabla}_s = (\underline{\underline{I}} - \underline{n}\underline{n}) \cdot \underline{\nabla}. \tag{8}$$

Taking the tangential and normal to the free surface components of this force balance, we obtain

$$\underline{t}\underline{n} : \underline{\underline{\sigma}} = 0, \tag{9a}$$

$$\underline{n}\underline{n} : \underline{\underline{\sigma}} = \frac{2H}{\mathrm{Ca}}. \tag{9b}$$

On the surface of the disk or the internal pipe wall, the usual no-slip and no penetration conditions are imposed,

$$\underline{t} \cdot \underline{v} = 0, \quad \underline{n} \cdot \underline{v} = 0. \tag{10}$$

In addition, either on the plane of symmetry $z=0$ for the radial flow or on the axis of symmetry $r=0$ for the pipe flow, we impose the typical boundary conditions for flow symmetry

$$\underline{n} \cdot \underline{v} = 0, \quad \underline{t}\underline{n} : \underline{\underline{\sigma}} = 0. \tag{11}$$

As far as the inflow boundary is concerned, we consider that there the flow is 1D and, thus, the tangential component of the velocity vector is zero,

$$\underline{t} \cdot \underline{v} = 0. \tag{12}$$

At the same location, we impose a constant value on the pressure from the start of the flow, since this is the examined type of flow, using the open boundary condition proposed by Papanastasiou *et al.* (1992). We should mention here that the value of the dimensionless pressure P_{in} is determined by requiring that the dimensionless velocity at the tip of the air-liquid interface at $t=0^+$ is equal to unity, since the initial tip velocity is used as a characteristic velocity. Finally, the model is completed by assuming that for both problems the fluid is at rest initially, $\underline{v}(r,z,t=0)=0$.

III. NUMERICAL IMPLEMENTATION

In order to numerically solve the governing equations and accurately simulate both flows, we chose the mixed finite element method combined with an elliptic grid genera-

tion scheme for the discretization of the deforming physical domain. This method was combined with mesh refinement to resolve the flow, where this is needed the most as well as with occasional mesh reconstruction, to improve the spatial discretization when it was necessary.

A. Elliptic grid generation

We use a set of partial differential equations, the solution of which generates a boundary-fitted discretization of the deforming domain occupied by the liquid. This method was developed by Dimakopoulos and Tsamopoulos (2003b) and was successfully applied in various complex flows, involving free surfaces undergoing large deformations [Dimakopoulos and Tsamopoulos (2003a); Dimakopoulos and Tsamopoulos (2007); Karapetsas and Tsamopoulos (2006); Tsamopoulos *et al.* (2008)]. Here, we will only present our adaptation of its essential features to the current problem. The interested reader may refer to Dimakopoulos and Tsamopoulos (2003b) for further details on all the important issues of the method. With this scheme, the time-dependent physical domain is mapped onto a fixed with time computational one. The mapping depends on the flow geometry,

- $(r,z)\rightarrow(\xi,\eta)$, for the pipe flow,
- $(z,r)\rightarrow(\xi,\eta)$, for the flow between parallel disks.

A fixed computational mesh is generated in the latter domain, while, through the mapping, the corresponding mesh in the physical domain follows its deformations. As initial computational domain for each geometry, we choose here the initial control volume defined above. This mapping is based on the solution of the following system of quasi-elliptic partial differential equations,

$$\underline{\nabla}\cdot\left(\varepsilon_1\sqrt{\frac{r_\xi^2+z_\xi^2}{r_\eta^2+z_\eta^2}}\underline{\nabla}\xi+(1-\varepsilon_1)\underline{\nabla}\xi\right)=0, \tag{13}$$

$$\underline{\nabla}\cdot\underline{\nabla}\eta=0, \tag{14}$$

where ε_1 is a parameter that adjusts the orthogonality of the resulting mesh; its value is chosen by trial and error, and here it is set to 0.1. The mesh in the physical domain deforms, with a velocity which is not necessarily equal to the local fluid velocity, and therefore this method belongs to the group of arbitrary-Langrangian-Eulerian methods. The solution of these differential equations requires the imposition of the appropriate boundary conditions. In both problems, along the moving interface we impose the kinematic equation,

$$\frac{D\underline{F}}{Dt}=\underline{v}, \tag{15}$$

where $\underline{F}=r\underline{e}_r+z\underline{e}_z$ is its position vector, together with a condition to uniformly distribute the interfacial nodes. On each of the remaining boundaries, which are fixed, two conditions are imposed. The first one determines their position, while the other one distributes uniformly the nodes along the boundary line. Either an algebraic distribution or the penalty method is applied for that purpose [see Dimakopoulos and Tsamopoulos (2003b)].

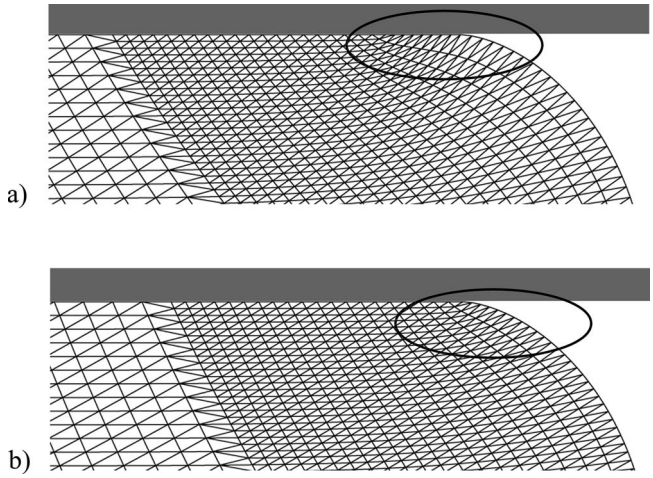

FIG. 2. Schematic representation of the remapping scheme of the interfacial nodes (a) before and (b) after the procedure.

B. Global mesh reconstruction

The free surface of the fluid becomes highly deformed as the fluid advances with time. Parts of it come very close to the solid wall and, possibly, into contact with it. Therefore, a new triple contact point is created ahead of the previous one. In order to deal with this problem, we adapted the method first described by Behrens *et al.* (1987) and Mavridis *et al.* (1988) and later on advanced by Poslinski and Tsamopoulos (1990, 1991), Karapetsas and Tsamopoulos (2006) and Dimakopoulos and Tsamopoulos (2007) to model the motion of the contact line in transient flows when the capillary number is very large, as in the present case. This makes capillary forces insignificant when compared to viscous forces and the apparent contact angle equals 180°. Thus, at start up the interface, which is initially perpendicular to the wall, deforms and the contact angle increases, while the no-slip condition keeps the contact line fixed. When the contact angle becomes 180°, points from the advancing interface come in contact with the wall and the contact line effectively moves. This implies a rolling motion of the liquid around the contact line, which is occupied by a different material point as it translates downstream. Different adjustments of the time stepping and treatment of the collision of material points with the wall have been employed in the above papers without an appreciable effect. Having used a much smaller and adjustable time step, we found that, in Newtonian fluids, only the node, which is nearest to the wall, simply approached it with a very small velocity because of the no-slip condition at the neighboring contact point. This nearest point never surpassed the wall and was considered attached to it when the distance from it was less than 10^{-4}. Consequently, we managed to retain the no-slip condition on the wall and allowed the flow kinematics near it to dictate the advancement of the contact point.

A consequence of this rolling motion is that as time passes, more nodes collide with the wall making the discretization of the free surface coarser. The importance of this adverse effect increases with time, especially for those simulations that proceed to very long times. In order to overcome these difficulties, we have developed a mesh reconstruction scheme. The goal is for the free surface to retrieve all its nodes that collided with the bounding wall and to attain again its original element density. In Fig. 2, we highlight the differences of a mesh before and after the reconstruction procedure. As one

can clearly notice in Fig. 2(a), the free surface has been deformed and its discretization has become coarser because eight of its elements have collided with the wall. In Fig. 2(b) it is shown that, after the mesh reconstruction, these eight elements became again part of the free surface and the mesh in the contact point region became less distorted. This procedure is applied after a certain number of nodes, have collided with the wall and before the free surface has lost too many nodes, in order to preserve the accuracy of our computations. Typically, this occurred after one element collided with the wall, but this number could be adjusted up to eight elements. At the chosen time step, time integration is paused until the generation of the new mesh is completed and the values of the solution vectors are assigned to the new locations of the nodes.

The basic steps of this procedure are:

(a) Define the new computational domain to extend from the position of the inflow boundary to the current location of the triple contact point.

(b) Reconstruct the new mesh in the physical domain by solving the elliptic mesh generation equations and applying as boundary conditions the position of all boundaries. As initial guess, the new computational domain is used. The position of the fixed boundaries is known and simple algebraic equations are applied for the equal distribution of the nodes along them. The procedure for the free surface nodes, though, is not as simple: in the perpendicular to flow direction, the nodes are placed in the position they had just after the previous remeshing, i.e., the initial number of nodes on the front is restored. Given this position, we use interpolation techniques to calculate from the old mesh the new positions of the nodes in the flow direction. It was found that this is a good way to achieve a uniform distribution of the nodes on the free surface during the remeshing. However, we should note here that for these calculations, a continuation procedure is needed in order to achieve convergence, since the computational mesh is not a very good initial guess for the new mesh in the physical domain.

(c) Compute the values of velocity and pressure vectors at the new grid points using interpolation and search techniques between the old and the new mesh.

C. Local mesh refinement

In order to increase the accuracy of the solution in the region near the deforming flow front and simultaneously reduce the computational cost, the *h*-refinement method has been used. The *h*-method was proposed by Szabo and Babuska (1991), who subdivided the elements in which the error measure was larger than a prescribed tolerance. Later, Tsiveriotis and Brown (1993) applied a non-conforming splitting of rectangular elements in a free boundary problem and argued that local mesh refinement is essential in cases where elliptic grid generators are used because this technique relaxes the requirements on the mapping equations and provides a greater flexibility on the handling of the grid. Alternatively, Chatzidai *et al.* (2009) developed and tested a conforming splitting of triangular elements to refine locally the mesh around a corner. This method has been adapted to the present problem. For further details about it and the benefits from using it in various flows, one may also refer to Chatzidai *et al.* (2009).

An example of the resulting mesh following this procedure in the present problem is shown in Fig. 3. Here, two levels of local refinement are shown for the case of a viscoplastic material flowing between two disks. As the material flows outward in the radial direction, it gets detached from the disk wall. Part of the fluid and the interface approaches the wall as the fluid advances but never comes into contact with the disk

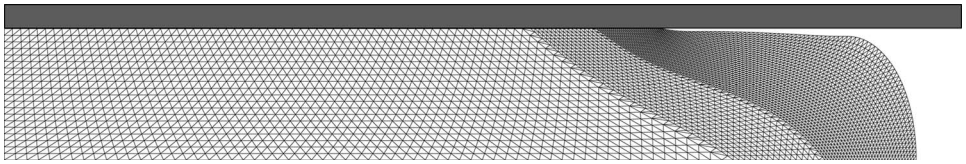

FIG. 3. Typical mesh with two levels of local refinement behind the advancing front for the flow between two disks with Bn=5, N=400, and P_{in}=53.13 at time t=3.33

surface (more details on this subject will be presented in Sec. IV). As time passes, the length of the free surface increases significantly resulting in an increased size of the elements at the interface, which could lead to loss of accuracy in our computations. When this type of interface deformation arises, the contact line does not move and the collision of nodes with the disk surface stops, rendering the mesh reconstruction technique, described earlier, useless. This makes the employment of the local mesh refinement scheme essential for our computations, since it allows assigning more nodes to the interface and the area around it without increasing excessively the overall computational cost. An additional benefit is the fact that we expect that unyielded material will arise near the free surface due to the low stresses that the fluid experiences there and the refined mesh will help in resolving the yield surface more accurately.

D. Mixed finite element method

The discretization of the flow and mesh equations is performed using the mixed finite element/Galerkin method. The computational domain is discretized using triangular elements as already described. We approximate the velocity and position vectors with six-node Lagrangian basis functions ϕ^i and the pressure with three-node Lagrangian basis functions ψ^i.

Applying the divergence theorem, the weak form of the momentum balances is given as

$$\int_{\Omega}\left[\mathrm{Re}\frac{D\underline{v}}{Dt}\phi^i+\nabla\phi^i\cdot\underline{\underline{\sigma}}\right]\mathrm{d}\Omega+\int_{\Gamma}[\underline{n}\cdot\underline{\underline{\sigma}}]\phi^i\mathrm{d}\Gamma=0, \tag{16}$$

while the weak form of the mass balances is

$$\int_{\Omega}\psi^i\nabla\cdot\underline{v}\mathrm{d}\Omega=0, \tag{17}$$

where $\mathrm{d}\Omega$ and $\mathrm{d}\Gamma$ are the differential volume and surface area, respectively. The boundary integral that appears in the momentum equations is split into four parts, and each one of them corresponds to a boundary of the physical domain and the relevant boundary condition is applied therein. More specifically, the term of the surface integral that corresponds to the interface involves second order derivatives, through the definition of the mean curvature H. In order to avoid dealing with them, we have used an equivalent formulation for it,

$$2H\underline{n}=\frac{d\underline{t}}{ds}-\frac{\underline{n}}{R_2}, \tag{18}$$

where the first term describes the change of the tangential vector along the free surface and R_2 is the second principal radius of curvature. At the remaining boundaries, the

TABLE I. Properties of the finite element meshes used in this paper.

Mesh	Initial number of 1D elements		Levels of local refinement	Number of 1D elements on the free surface	Number of triangular elements	Total number of unknowns
	ξ -direction	η -direction				
M1	20	80	2	80	9020	78133
M2	30	60	1	60	6870	59507
M3	30	60	2	120	13410	115529

momentum balances are replaced by the essential conditions imposed therein.

The weak form of the mesh generation equations is derived in a similar way applying the divergence theorem,

$$\int_{\Omega} \left(\varepsilon_1 \sqrt{\frac{r_\xi^2 + z_\xi^2}{r_\eta^2 + z_\eta^2}} + (1 - \varepsilon_1) \right) \underline{\nabla} \xi \cdot \underline{\nabla} \phi^i \mathrm{d}\Omega = 0, \tag{19}$$

$$\int_{\Omega} \underline{\nabla} \eta \cdot \underline{\nabla} \phi^i \mathrm{d}\Omega = 0. \tag{20}$$

E. Solution procedure

The resulting set of discrete equations is integrated in time with the implicit Euler method. An automatically adjusted time step is used for that purpose, which ensures the convergence and optimizes code performance [Dimakopoulos and Tsamopoulos (2007)]. The final set of algebraic equations is non-linear and an iterative solver has to be used. In particular, they are solved in each time step using a two-step Newton–Raphson/non-linear Gauss–Seidel iteration scheme, which decouples the flow equations from the mesh generation equations. The former ones are solved first on the grid points of the physical domain determined from the previous time step until convergence, and the computed flow variables are used for the solution of the spatial equations. The iterations of the Newton–Raphson method are terminated using 5×10^{-10} as tolerance for the absolute error of the residual vector. This is an effective method because it results in significantly smaller Jacobian matrices, which are easier to handle. The Jacobian matrices that are generated are stored in a compressed sparse row format [Saad (2000)], and the linearized system is solved by Gaussian elimination using PARDISO, a robust, hybrid, and sparse matrix-solver [Schenk and Gärtner (2004); Schenk *et al.* (2000)]. A number of convergence tests have shown which mesh is sufficient to give accurate results in either geometry for the various Bingham numbers used. The selected meshes are shown in Table I. Meshes M2 and M3 were used for the pipe flow. The former mesh was used for a Newtonian fluid or materials with low Bingham numbers (e.g., Bn=0.5). At higher Bingham numbers leading quite early to detachment of the fluid from the pipe wall, a more refined mesh near the free surface is needed and, as such, mesh M3 was found to be satisfactory. In radial flow between parallel disks, even the initial flow domain is larger in the radial direction requiring the finer mesh M1 for all the simulations. The initial time step for all the simulations was $\Delta t = 10^{-5}$. The codes were written in FORTRAN 90 and were run on a workstation with dual Xeon CPU at 2.8 GHz in the Laboratory of Computational Fluid Dynamics. Each run typically required 4–5 days to complete.

F. Yield surface determination

Using the exact Bingham model, the shape and location of the yield surface can be obtained by two criteria: it is either the contour surface where the second invariant of the rate of strain tensor equals zero $\dot{\gamma}=0$, or the one where the second invariant of the stress equals the Bingham number $\|\underline{\underline{\tau}}\|=\mathrm{Bn}$. However, it is clear that these two criteria are not equivalent using the Papanastasiou model. This is because this constitutive model is differentiable and predicts small but non-zero values of $\dot{\gamma}$ for regions, where $\|\underline{\underline{\tau}}\|<\mathrm{Bn}$. Therefore, in this case the only acceptable criterion is the second one [Dimakopoulos and Tsamopoulos (2003a)]. The main differences between these two criteria were also extensively discussed by Karapetsas and Tsamopoulos (2006). According to the second one, the material yields when the second invariant of the stresses exceeds the yield stress, which is summarized by the following:

$$\text{yielded material:} \quad \|\tau\| > \mathrm{Bn}, \tag{21a}$$

$$\text{unyielded material:} \quad \|\tau\| \leq \mathrm{Bn}. \tag{21b}$$

In order to calculate the second invariant of the stresses, the gradient of the velocity is needed. The latter, however, is discontinuous at the sides of each element of the mesh, and its calculation directly at the nodes is not possible. A nice way to overcome this difficulty is to obtain a continuous approximation of the extra stress tensor using the Galerkin projection method,

$$\int_{\Omega} \phi_i(\underline{\underline{T}} - \underline{\underline{\tau}})\mathrm{d}\Omega = 0, \tag{22}$$

where $\underline{\underline{T}}$ stands for the continuous approximation of the stress tensor $\underline{\underline{\tau}}$. A similar procedure is followed to obtain contours of $\dot{\gamma}$.

IV. RESULTS AND DISCUSSION

A parametric analysis for both flow arrangements is presented here. The qualitative changes in their main characteristics as the yield stress increases are the outstanding features in the present study. In Sec. IV A, we present results for the pipe flow, while in Sec. IV B we present results for the flow between two parallel disks.

A. Flow inside a cylindrical pipe

To set the stage for the discussion that follows, it is useful to examine first the evolution of certain variables when a Newtonian fluid, i.e., Bn=0, flows inside a straight pipe. Taking the initial length of the control volume as $l=4$ leads to a dimensionless applied pressure at the inlet boundary of $P_{\mathrm{in}}=16.45$. As an indicative value of the weak capillary effects, we take $\mathrm{Ca}=10^3$ in this and all subsequent simulations. The upper and lower halves of Fig. 4 illustrate the contour lines of the radial and axial velocities, respectively, at three time instants. The left and right boundaries of each plot correspond to the inflow boundary and the fluid/air interface, respectively. We observe that the free surface, which was initially flat, deforms everywhere and that, after its initial development, it retains its shape even at large times. As expected, the computed flow to some extent from the inflow boundary is 1D and it is in quantitative agreement with the analytical solutions for fully developed Poiseuille flow in a pipe [Bird *et al.* (1960)]. Indeed, the pressure difference we calculate between $z=0$ and $z=2$, where the flow should be fully developed, is $\Delta P=3.727$ at time $t=15.83$. Using this pressure gradient in

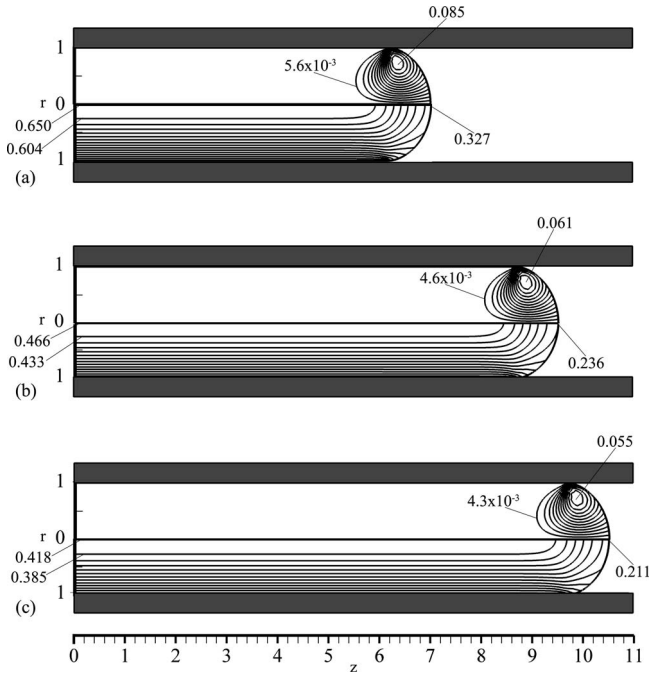

FIG. 4. Contours of the radial, upper half, and the axial, lower half, velocity component of a Newtonian fluid in a straight pipe at (a) $t=6.62$, (b) $t=15.83$, and (c) $t=20.36$ for $(\mathrm{Ca},\mathrm{Bn},l,P_{\mathrm{in}})=(10^3,0,4,16.45)$. The interval between the max and min v_z in each snapshot was divided by 16, 15, and 14 contour lines, respectively. The number of contour lines for v_r in each of the three snapshots is 16, 14, and 14, respectively. The M2 mesh was used.

the expression for Poiseuille flow yields a maximum axial velocity of $U_{\max}=0.466$, which is identical to the value calculated from our simulations. This test is a direct validation of our code.

Closer to the free surface, however, the flow becomes 2D. At every instant, the axial velocity takes its maximum value at the intersection of the inflow boundary with the axis of symmetry, and this value remains constant along the axis of symmetry up to an axial position about two radii behind the tip. However, radially its value monotonically decreases toward its minimum (zero) value at the pipe wall, where the no-slip condition is imposed. We notice that the velocity decreases with time throughout the domain. The deceleration of the flow is expected because during the simulation we impose a constant pressure drop on increasing amounts of fluid in the expanding control volume, which increase the viscous resistance. As for the radial velocity, it takes non-zero values only close to the liquid-air interface. Its maximum value is located near the contact line. There, the material is displaced slowly toward the pipe wall and the aforementioned wetting process of the pipe takes place. Moreover, we observe that the radial velocity is one order of magnitude smaller than the axial one and decreases with time as well. In fact in fountain flow and near the flow front, the radial velocity is of the same order of magnitude as the difference between the axial velocity and its average value. The radial velocity takes negligible values in the rest of the domain, verifying that the flow there is 1D. Similarly, the pressure as well as the stress variation is 1D far away from the free surface. The variation in the shear stress τ_{rz} and the pressure are shown on the lower and upper half of the domain in Fig. 5, respectively. This snapshot is taken at time $t=15.83$ [same

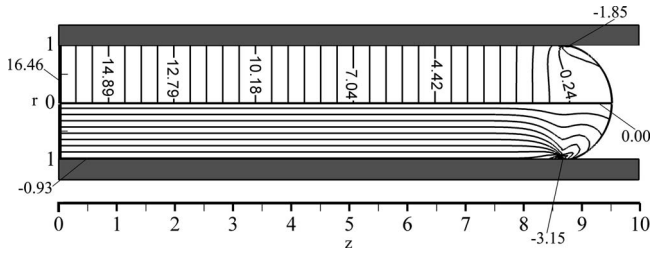

FIG. 5. Contours of the pressure field, upper half, and τ_{rz}, lower half of a Newtonian fluid at time $t=15.83$ for $(\mathrm{Ca},\mathrm{Bn},l,P_{\mathrm{in}})=(10^3,0,4,16.45)$. There are 31 contour lines for τ_{rz} and 36 contour lines for the pressure.

as Fig. 4(b)]. We observe that the pressure depends only on the axial direction almost up to the triple contact point and that τ_{rz} exhibits a strong singularity at that point where the transition from the no-slip to the shear-free condition at the interface of the fluid takes place. Away from the liquid front, the distances between the P or the τ_{rz} contours are equal, verifying that in Newtonian liquids the pressure or the shear stress depend linearly on the axial and the radial distance, respectively. The τ_{rz} contours bend toward the triple contact point, as they approach the liquid front.

In order to validate further our numerical code, we compared our simulation results with the experimental data provided by Behrens *et al.* (1987) for Newtonian fluids as well, advancing in straight cylindrical tubes. The comparison is demonstrated in Fig. 6. These data relate the axial distance between the flow front tip and the triple contact point z_{tip}-z_c, with the axial displacement of the front tip z_{tip}-$z_{\mathrm{tip,init}}$. Although a constant flow rate was maintained in the experiments, our numerical results show very good agreement with their data, indicating that the front shape is not affected by the condition driving the flow. Initially, the interface is flat and the triple contact point has the same axial position with the tip. Subsequently, the difference of these two positions increases as the free surface deforms, while at larger axial tip positions it reaches asymptotically a constant

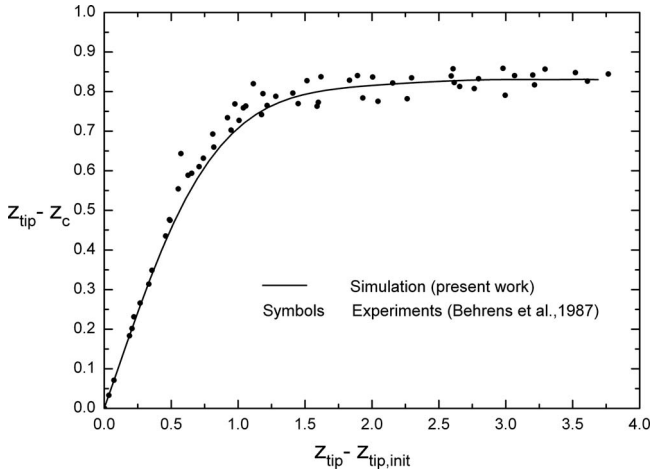

FIG. 6. Variation in the axial distance between the flow front tip and the triple contact point z_{tip}-z_c, with the axial position of the front tip z_{tip} for a Newtonian fluid in a straight pipe with $(\mathrm{Ca},\mathrm{Bn},l,P_{\mathrm{in}})=(10^3,0,4,16.45)$. Comparison with experimental data provided by Behrens *et al.* (1987). The same symbols have been used for all the experimental data, although the indicated variation is caused because the experiments took place with different fluids, pipe diameters, and flow rates.

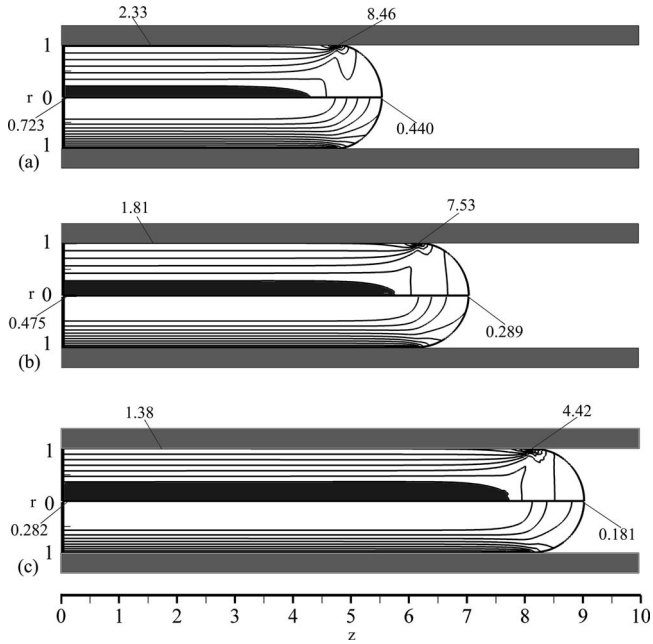

FIG. 7. Contours of the second invariant of the stresses, upper half, and the axial component of the velocity, lower half, of a viscoplastic fluid in a straight pipe at (a) $t=2.51$, (b) $t=6.80$, and (c) $t=15.68$. The dimensionless parameters are $(\mathrm{Ca},\mathrm{Bn},N,l,P_{\mathrm{in}})=(10^3,0.5,400,4,23.0)$. The range between the maximum and minimum value of v_z in each of the three snapshots was divided by 13, 11, and 10 contour lines, respectively. The number of isolines for the second invariant of the stresses in each snapshot is 28. The M2 mesh was used.

value, since the free surface acquires a constant pattern. It is known from experiments and earlier simulations inside a tube [Behrens *et al.* (1987)] that this constant value for z_{tip}-z_c is 0.83 ± 0.04 and that the front shape is nearly circular.

The effect of material viscoplasticity is shown in Fig. 7, the upper half of which gives the contours of the second invariant of the stress $\|\underline{\underline{\tau}}\|$, while its lower half gives the contours of axial velocity, at three time instances, for a relatively small Bingham number $\mathrm{Bn}=0.5$, while $N=400$. To set in motion the same amount of liquid as in the Newtonian case $l=4$ and under the same capillary forces, $\mathrm{Ca}=10^3$, requires a higher applied pressure $P_{\mathrm{in}}=23.00$ because of the material yield stress. The v_z contours are parallel to the tube wall far from the free surface but are bent toward the axis of symmetry or the interface in the same area that the radial velocity takes non-zero values, just as in the Newtonian case. Far from the interface, the only non-zero stress is the shear stress. However, it takes zero values on the axis of symmetry and, thus, unyielded material should arise in that area. The unyielded domains can be determined easily [see Eq. (21)] by computing the yield surface where $\|\underline{\underline{\tau}}\|=\mathrm{Bn}$. The upper half of each snapshot in Fig. 7 depicts the isolines of $\|\underline{\underline{\tau}}\|$ for values greater than the dimensionless yield stress $\mathrm{Bn}=0.5$, while the shaded areas indicate the unyielded material. Indeed, we notice that far from the interface, unyielded material arises in the core region of the pipe, surrounding the axis of symmetry, as expected. Closer to the interface, however, things are quite different: the contours of $\|\underline{\underline{\tau}}\|$, from nearly parallel to the tube walls, bend and intersect the axis of symmetry preventing the unyielded material from reaching the free surface of the fluid. We observe that the size of the unyielded domain grows significantly, as time passes both in the radial and in the axial directions. The evolution of the maximum radius and the axial length of the

TABLE II. Extent of unyielded region of a viscoplastic in a pipe material with Bn=0.5, N=400, and Ca=1000.

Time t	Maximum radius of core region	Length of core region
2.51	0.219	4.264
6.80	0.281	5.728
10.73	0.324	6.702
15.68	0.368	7.695

unyielded material is presented more clearly in Table II. The growth of the unyielded material in the axial direction is due to the axial displacement of the free surface as the fluid advances. On the other hand, its growth in the radial direction occurs because the fluid continuously decelerates and experiences ever decreasing stresses with time and, as a result, a larger part of the fluid experiences a stress magnitude lower than the yield stress of the fluid. For this small value of Bingham number and up to the time indicated, the material behaves similar to the Newtonian case: as the fluid advances in the pipe after the initial transient deformation, the cross section of its front remains nearly semicircular forming a constantly moving contact point. Although at the liquid front the tangential stress is identically zero, the fountain-like motion of the nearby material is strong enough, so that unyielded material, at least for the interval that the simulation lasted, does not arise here.

This simulation provides another possibility for a critical validation test of our code by comparing its predictions with the analytical solution given in Bird *et al.* (1960) for the fully developed flow inside a tube of a viscoplastic fluid, which follows the exact Bingham model. More specifically, Table III presents the differences in mean pressure ΔP calculated between the inflow boundary $z=0$ and $z=2$ at different times. Then the radius r_o of the unyielded region in the core of the tube is calculated analytically

$$r_o = \frac{2\mathrm{Bn}(\Delta z)}{\Delta P}, \tag{23}$$

while $r_{o,\mathrm{sim}}$ is the corresponding radius computed with the present simulation. One time instant was used also from the above results $t=15.68$ to analytically calculate the velocity profile at $z=2$,

$$v_z = 0.6910[1-r^2] - 0.5[1-r], \quad r_o \geq 0.3618,$$

$$v_z = 0.2814, \quad r_o \leq 0.3618. \tag{24}$$

TABLE III. Comparison of the radius of unyielded domain in a pipe at various time instants between the analytically predicted value r_o and the calculated one using the present code $r_{o,\mathrm{sim}}$ for a material with Bn=0.5, N=400, and Ca=1000.

Time t	Pressure drop ΔP	r_o	$r_{o,\mathrm{sim}}$ at $z=2$
2.51	9.3697	0.2135	0.2179
6.80	7.2503	0.2759	0.2798
15.68	5.5282	0.3618	0.3641

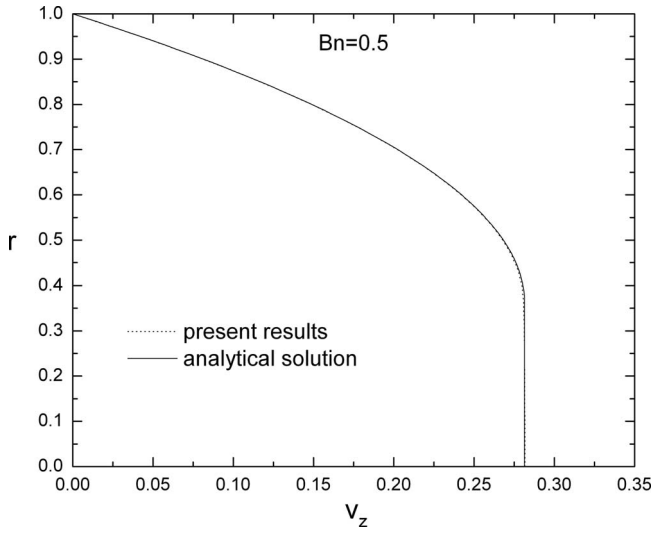

FIG. 8. Comparison of the analytical prediction for the axial velocity profile with numerical simulation along $z=2$ with $\Delta\bar{P}=5.5282$ at $t=15.68$ for Bn=0.5.

The comparison of the analytical velocity profile with the solid line [Eq. (24)] and the velocity profile extracted from the data of the simulation with the dotted line are shown in the Fig. 8. The two curves coincide except for a small area around the bending of the profile at $r_o=0.361\,8$, verifying not only the accuracy of the present simulations but also that the value of the exponential parameter we chose was large enough, so that the predictions of the two models are identical.

Increasing the material yield stress introduces a very interesting departure from this picture. Figure 9 illustrates the injection of a viscoplastic fluid with Bn=3 and $N=300$. The increased material yield stress requires an even higher applied pressure $P_{\text{in}}=52.17$ to give to the same amount of material and the same capillarity the value of unity to the initial dimensionless tip velocity. The figure gives $\|\underline{\underline{\tau}}\|$, on its upper part, and pressure, on its lower part, at three time instants. From the first snapshot of this figure at $t=1.38$ [Fig. 9(a)], we deduce that at very early times the contact point has moved slightly following the motion of the liquid front. Indeed, the axial position of the triple contact point is at $z_c=4.17$, while initially it was at $z_c=4$. However, after this instant the material interface closer to the wall becomes nearly parallel to it. As more and more fluid enters the control volume, the front advances but clearly it remains detached from the tube wall leaving the contact line stationary. We should note here that as the simulation proceeds, the length of the free surface increases significantly. It is characteristic that at time $t=8.23$, the total length of the cross section of the free surface has almost quintupled from its initial value at start up. This makes apparent the need for a local refinement scheme near it in order to assign more nodes to the free surface and retain the desired accuracy of our computations without increasing excessively the overall computational cost.

The unyielded material is represented by the shaded areas, in the upper half of each snapshot in Fig. 9. We observe that unyielded material arises both in the core region of the tube as with Bn=0.5, but now also in the region close to the free surface. With Bn =3 and while the interface deforms from flat to curved, the flow field is strong enough near the liquid front to keep the stress in the material near it above its yield value. However, when the front only slightly deforms from its curved shape, the small stresses

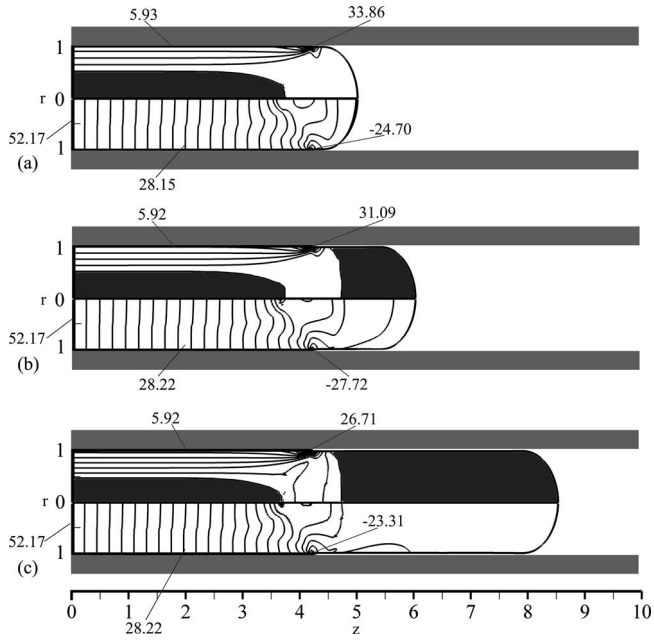

FIG. 9. Contours of the second invariant of the stresses, upper half, and the pressure field, lower half of a viscoplastic fluid at (a) $t=1.38$, (b) $t=3.33$, and (c) $t=8.23$ for $(\mathrm{Ca},\mathrm{Bn},N,l,P_{\mathrm{in}})=(10^3,3,300,4,52.17)$. In each of the three snapshots, we have plotted 40 isolines for $\|\underline{\underline{\tau}}\|$ and 30 isolines for the pressure. The M3 mesh was used.

that the fluid experiences near it are not sufficient to overcome the yield value and an unyielded material is formed there. It should be reminded here that the movement of the contact line is due to a spilling motion of fluid from the advancing front because the contact point remains fixed in space while it is overtaken by fluid from the front. All these increase locally the material viscosity and prevent new viscoplastic material, moving in fountain-type flow, from approaching the contact point, and leading to detachment. From that instant onward, the material behind the front advances as a solid and the unyielded region right behind the material front grows axially following it in its motion, while its left point at the axis of symmetry remains at about the same position $z\approx 4.6$. Starting from that point, the yield surface bends back toward the triple contact point but remains ahead of it. Therefore, as the material passes the region of the contact point, it becomes detached from the wall and solid-like and, hence, it maintains its steady motion without consuming additional energy to do so. Thus, the viscous resistance at the pipe wall does not increase, since the fluid in contact with the wall does not increase either. In other words, although the material ahead of the contact point increases, its unyielded condition prevents the flow from developing any more. For this reason, the area of the unyielded material in the core region of the tube does not change significantly with time, in contrast to the previous simulation with $\mathrm{Bn}=0.5$. This can be readily seen in Table IV, where $r_{o,\mathrm{sim}}$ for the two time instants 3.33 and 8.23, when the detachment had already occurred, remains the same at 0.5194. Similarly, after it reaches $z_c=4.17$, the triple contact point does not move. The material detachment from the wall and the high values of stress that are retained around the contact point stop the translation of the yield surfaces toward each other and prevent them from merging. The radial growth of the unyielded domain in the core region of the fluid for $\mathrm{Bn}=0.5$ occurs because of the deceleration of the flow.

TABLE IV. Comparison of the radius of unyielded domain in a pipe at various time instants between the analytically predicted value r_o and the calculated one using the present code $r_{o,\mathrm{sim}}$ for a material with Bn=3, N =300, and Ca=1000.

Time t	Pressure drop ΔP	r_o	$r_{o,\mathrm{sim}}$ at $z=2$
1.38	23.8192	0.5038	0.5199
3.33	23.7466	0.5053	0.5194
8.23	23.7541	0.5052	0.5194

Deceleration, however, for Bn=3 does not take place, as explained above. To verify this new picture, Fig. 9 demonstrates that along the tube wall $\|\underline{\underline{T}}\|$ is nearly constant throughout the simulation and in spite of the large advancement of fluid in the tube. This confirms that the variation of the viscous forces opposing the constant applied pressure difference is negligible and the fluid does not decelerate as in the previous two simulations, but it retains an almost steady flow rate. The flow around the triple contact point remains invariant after detachment producing a plug of constant radius ahead of it.

As for the pressure shown in the lower part of Fig. 9, we notice that it exhibits a strongly 2D character at the axial position near the triple contact point and between the two unyielded domains. Moreover, we observe that even closer to the inflow boundary the contours of pressure are not straight lines showing a weak dependence on the radial direction in contrast to the Newtonian solution. At long times, the pressure shows very small variation near the free surface, as expected, due to the plug-like flow in that area. In addition, the variation of pressure does not change significantly among the three time instants shown in the figure. For example, at the position with coordinates (r,z) $=(0.96,2.00)$, the value of pressure changes very slightly taking successively the values 28.15, 28.22, and 28.22. This is not surprising since viscous resistance to flow does not increase with time.

The time evolution of the shape of the fluid/air interface is illustrated more clearly in Fig. 10 for the two Bn values. The interface of the material with Bn=0.5 retains a nearly semi-circular profile. Closer examination reveals that it slowly becomes straighter near the wall and bends more abruptly at a small distance from it. In addition, the distance z_{tip}-z_c increases slowly with time. In contrast to this when Bn=3, the triple contact point, after a small initial movement, remains stationary while the free surface deforms and continues to advance. Looking more closely, we observe that just ahead of the contact point the free surface bents slightly away from the tube wall, and, subsequently, becomes almost parallel to it. It seems that the free surface in this part does not expand in the radial direction at all, keeping constantly the circumference of the material at a tiny distance from the wall. At an ever-increasing distance from the contact point, this part of the interface turns slightly toward the wall becoming convex without, however, reaching it and, finally, sharply turns toward the axis of symmetry. This is the part of the material that first became unyielded at its front and its shape is reminiscent of the fountain-type flow that was taking place there before the yield condition was not satisfied.

In order to examine the mechanism leading to detachment further and see if any changes occur in the flow characteristics before and after it, first we examined the velocity field. For example, we compared the values of the tip velocity vs. the plug velocity of the upstream flow of a material with Bn=3 at three time instances (one well before, one close to, and one after detachment), but we did not observe anything special happening. Then, we examined whether the stresses undergo a qualitative change when detachment

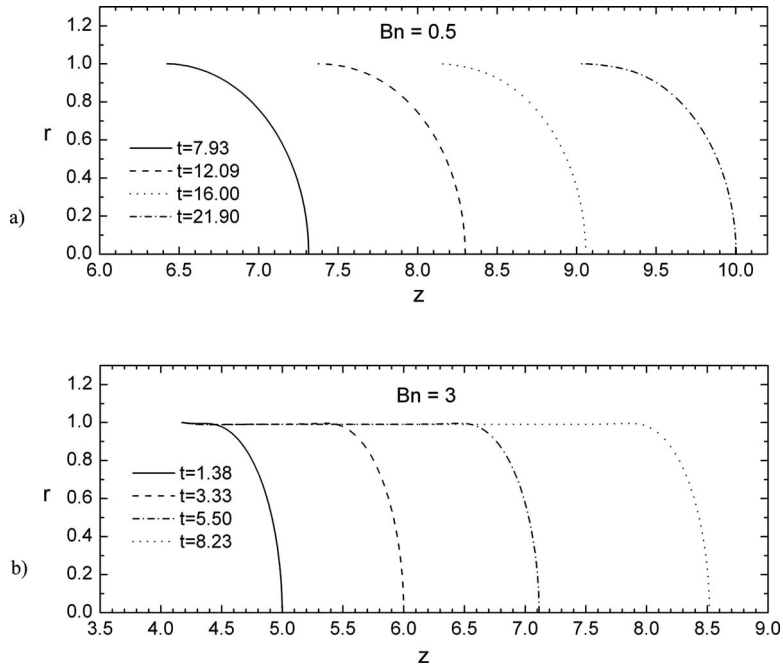

FIG. 10. Time evolution of the shape of the fluid/air interface for a viscoplastic material with (a) Bn=0.5 and (b) Bn=3. The rest dimensionless parameters are (a) $(\mathrm{Ca}, N, l, P_{\mathrm{in}}) = (10^3, 400, 4, 23.0)$ and (b) $(\mathrm{Ca}, N, l, P_{\mathrm{in}}) = (10^3, 300, 4, 52.17)$.

occurs. We focused on the radial normal stress because this is the component that could induce detachment from the wall. Indeed, we found out that τ_{rr} takes negative values around the contact point, the magnitude of which is maximized at the contact point assuming larger values than any other stress component. This occurs before detachment, but it becomes more pronounced during and after it. Near the contact point and in Newtonian fluids, τ_{rr} also takes negative values; but on the contrary to viscoplastic fluids their magnitude decreases with time and separation does not take place. Clearly, it is the increase in the plastic contribution to the effective viscosity in viscoplastic materials induced by the reduction of $\dot{\gamma}$ near the contact point, which leads to the increase in the absolute values of τ_{rr} and finally to detachment.

It would be interesting to see the effect of separation on the flow rate. To this end, we have plotted the evolution of the velocity at the tip of the interface $V_{z,\mathrm{tip}}$ for various Bn values in Fig. 11. The curve of $V_{z,\mathrm{tip}}$ for the Newtonian fluid is concave starting from unity and monotonically decaying, showing clearly the decelerating nature of the flow. For small values of Bn (Bn=0.5 and Bn=1), this curve is similar to the Newtonian one, at least for the duration of these simulations. We observe that at early times the smaller the Bn, the smaller is the rate of deceleration because of the lower material viscosity generated by the initially higher rate of strain. However, at time $t \approx 2.19$ the curve for the two viscoplastic fluids clearly falls below the Newtonian curve, which means that the viscoplastic material starts to decelerate faster than the Newtonian one. Increasing further the yield stress of the material has a significant effect on the tip velocity. For Bn=2, initially, the free surface tip decelerates almost as fast for the Newtonian fluid and, at $t \approx 2.48$, it has decreased from unity to 0.444. After that instant, the tip velocity remains constant with time and equal to this value, indicating that the flow rate of the material

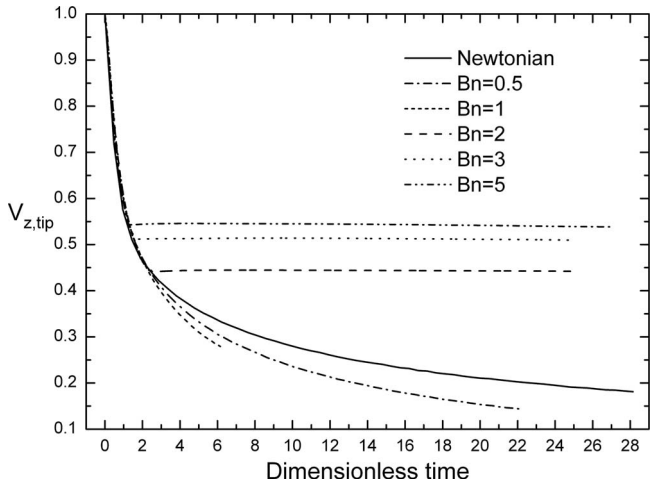

FIG. 11. Time evolution of the axial component of the velocity at the interface tip $V_{z,\text{tip}}$ for various Bn. The rest of the dimensionless parameters are $(\text{Ca}, l)=(10^3, 4)$.

becomes steady. Just before the curve turns to become parallel to the horizontal axis, the material has been detached from the tube wall, as described earlier (see Fig. 9), and the flow proceeds with almost constant shear forces exerted on the material. In other words, after detachment this pressure driven flow is simultaneously one with constant flow rate and, conversely, if a constant flow rate had been imposed, after detachment, it would require a constant pressure drop not an increasing one. Similar behavior is observed for the materials with Bn=3 and Bn=5. It is also shown for these cases that as Bn increases, the constant velocity attained by the material increases. This occurs because the higher the yield stress is the earlier detachment of the fluid occurs, leaving a smaller contact area with the wall, and, consequently, the higher the velocity that the material retains.

It is interesting to present the deformation of the front by plotting the axial distance between the flow front tip and the triple contact point z_{tip}-z_c versus the axial position of the front tip, z_{tip}, for various Bn numbers and compare this variation with the well-established one for Newtonian fluids (see Fig. 6). This is shown in Fig. 12. Clearly, for a material with low viscoplasticity (Bn=0.5), the difference of these two positions initially increases, as the free surface starts to deform, reaching, however, a very slowly increasing value after some time above the Newtonian limit. On the other hand, for more viscoplastic materials, this difference continues to increase indefinitely because as we have seen earlier, detachment of the fluid from the tube wall takes place and the fluid-air interface continuously lengthens.

Finally, two important questions remain: is there a critical Bingham number above which detachment occurs and does the material stop flowing when it does not detach from the wall? We tried to answer them by changing τ_y^*, as before, while keeping the same initial amount of fluid. Unfortunately, such attempts were not successful for various reasons. For example, while trying to approach the critical Bn we observed that the material tended to form inclusions in the scale of an element, irrespective of the mesh size or the size of the time step. Including such effects would require extensive modifications of our code. Also, while trying to determine a stopping time, our computations would require very long times and the contact point would translate so far that the mesh we could afford to use would not suffice to accurately calculate the flow field and $\dot{\gamma}$ would decrease so much that would require a considerable increase of N. Then we

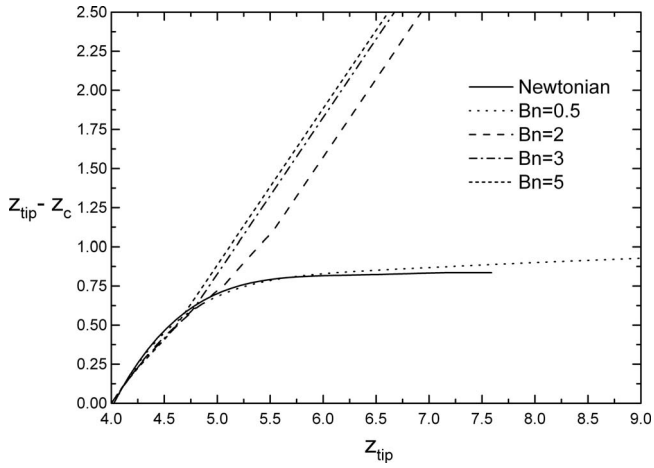

FIG. 12. Variation in the axial distance between the flow front tip and the triple contact point z_{tip}-z_c, with the axial position of the front tip z_{tip} for various Bn numbers in a straight pipe.

pursued a different route: we kept the material yield stress and the applied pressure the same, while we decreased/increased the amount of liquid initially in the control volume. Naturally, this increases/decreases the dimensional velocity and, hence, decreases/increases Bn, considerably whereas the value of $\overline{\text{Bn}}$ remains a constant. Interestingly, plotting in Fig. 13 the detachment length vs. the initial length for $\overline{\text{Bn}}=0.068$, we found out that all points fall on a line with slope less than 45°. This line intersects the $y=x$ line at $z_{c,\text{init}} \simeq 5.3$, where $\text{Bn} \simeq 17.8$. It was not possible to carry out calculations for so large Bingham numbers, even after lowering the value for the exponent at the Papanastasiou model to $N=100$. We anticipate that at this point, the material will detach from the wall without advancing at all. We repeated similar calculations for $\overline{\text{Bn}}=0.057$ and produced a line slightly above and nearly parallel to the previous one intersecting the $y=x$ at somewhat larger $z_{c,\text{init}} \approx 6$ with similar Bn. Therefore, for the same $\overline{\text{Bn}}$, the position that the

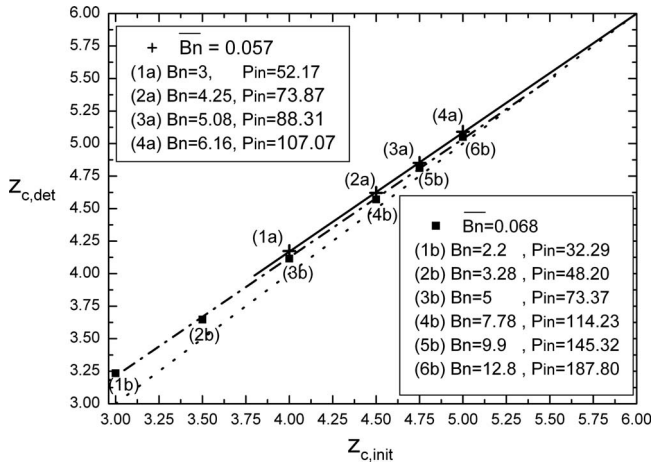

FIG. 13. Dependence of the location of the triple contact point at detachment on its initial axial position for two sets of Bn numbers, each corresponding to a single $\overline{\text{Bn}}$, for pipe flow. The slope of the line with $\overline{\text{Bn}}=0.057$ is 0.915, whereas the slope for $\overline{\text{Bn}}=0.068$ is 0.918.

fluid detaches depends linearly on the initial length. From these calculations, we conclude that separation will always take place and that the larger the Bingham number (up to Bn=12.8 for the case of $\overline{\mathrm{Bn}}$=0.068), the shorter the distance the contact point will translate before separation occurs. On the other hand, when Bn is quite small again separation should take place, but after the contact point has translated at very large distances. Therefore, neither a critical Bingham number nor a stopping time exists. Even when the Bingham number is very small, the fluid will advance considerably remaining in contact with the wall up to the point that it decelerates so much that unyielded material arises near the contact line leading to detachment.

Apparently, injection flow in a tube of a viscoplastic material is quite different from its steady 1D motion in a pipe. In the latter, no motion can take place, when the maximum value of the shear stress at the tube wall just becomes equal to the yield stress. Then the force balance between the pressure difference driving the flow $\pi R^{*2}\Delta P^*$ and the opposing wall stress $2\pi R^* L^*_{\mathrm{stop}}\tau^*_y$ provides an estimate of the "stopping" length $L^*_{\mathrm{stop}}=(R^*/2)\times(\Delta P^*)/(\tau^*_y)=(R^*/2)(1/\overline{\mathrm{Bn}})$. However, according to our previous predictions, this idea will work for injection flow as long as the fluid is not initially moving and will provide the max pressure gradient that can be applied to a viscoplastic material without initiating flow. On the contrary, when the fluid is already moving, there is no stopping length, since the fluid will continue to move with a decreasing velocity until it detaches from the wall and then it will assume a constant velocity. This difference is created by the 2D fountain-type flow at the front and around the contact point. The fluid deceleration along the axis of symmetry as it approaches the front tip and its subsequent radial acceleration turns the flow there to primarily elongational from simple shear away from the front. This has the detrimental implications we described above in the case of a viscoplastic material. The distance the contact point will travel decreases when Bn increases, for a given yield stress and pressure difference, i.e., the same $\overline{\mathrm{Bn}}$, indicating that the former definition is also more sensitive to the flow characteristics.

B. Radial flow between two parallel disks

We continue the discussion by presenting results for fluid injected between two parallel disks, first for the limiting case of a Newtonian fluid followed by those for a viscoplastic material. Setting the inflow boundary at a radial distance from the disks center of $l_1=3$, the liquid front at a radial distance from the inflow boundary of $l_2=5$ and the capillary number at the same high value $\mathrm{Ca}=10^3$ requires a dimensionless pressure of $P_{\mathrm{in}}=15.70$ to give the Newtonian liquid an initial dimensionless velocity at the tip of the moving front equal to 1. Figure 14 gives the evolution of the pressure, upper half, and of the radial velocity, lower half, at three time instants. The pressure decreases radially toward zero, the value of the air pressure ahead of the front, but at a decreasing rate [in contrast to the constant rate in pipe flow (Fig. 5)] because the increasing cross section here provides a smaller resistance to radial flow. As expected, pressure takes its maximum value at the inflow boundary and remains constant throughout the simulation, since it is imposed there, whereas it takes its minimum (negative) values in a very small region of the liquid around the contact point. Finally, it depends only on the radial coordinate in the major part of the flow field, but on both the radial and axial coordinates in a region extending radially about one disks' gap behind the free surface tip. According to Middleman (1977), who presented an analytical solution for the radial flow of a Newtonian fluid based on assumptions of lubrication theory, this dependence is with the natural logarithm of the radial coordinate. In order to validate once more our numerical code, we have plotted the pressure along the disk wall versus ln r (not shown here for conciseness) and

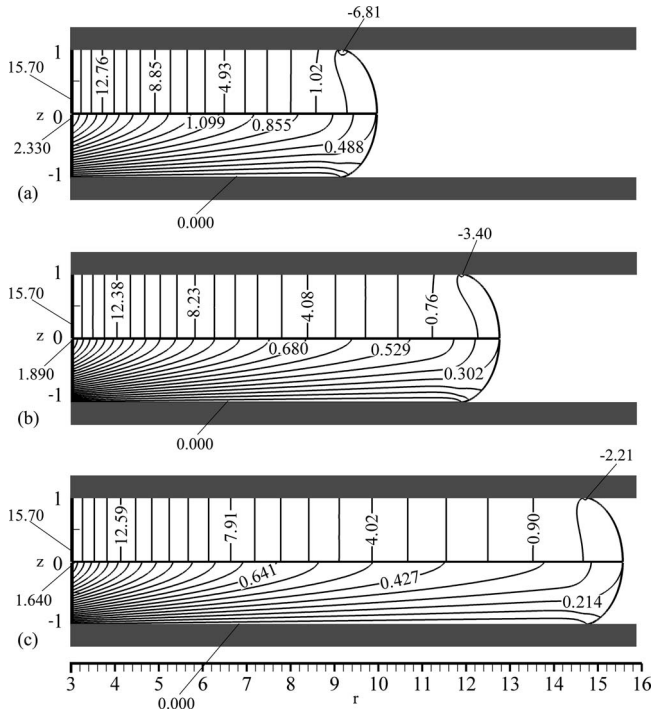

FIG. 14. Contours of the pressure field, upper half, and the radial velocity component, lower half, of a Newtonian fluid between two parallel disks at (a) $t=3.10$, (b) $t=10.55$, and (c) $t=21.79$ for $(\mathrm{Ca},\mathrm{Bn},l_1,l_2,P_{\mathrm{in}})=(10^3,0,3,5,15.70)$. The number of contours for the pressure in each of the three snapshots is 24. The interval between these two extremes in v_r is divided by 20, 26, and 24 contour lines in each of the three snapshots, respectively. The M1 mesh was used.

found a straight line in perfect agreement with theoretical predictions. The radial velocity has its maximum at the intersection of the inflow boundary with the plane of symmetry, and this value decreases with time due to the decelerating nature of the flow. Its minimum (zero) values appear on the disks surface, where the no-slip condition is imposed. All its contours begin from the inflow boundary and bend either toward the plane of symmetry or away from it intersecting the free surface. This bending of the primary velocity contours in the disk flow is in contrast to the straight contours of v_z in the pipe flow (compare with Fig. 4). This is because in a pipe, the velocity has only one component, which depends only on the transverse direction away from the liquid/air interface. The v_r contour line that emerges from the inflow boundary and ends at the free surface tip directly determines the decrease in the tip velocity from unity at start up to 0.488, 0.302, and 0.214 at the respective times of the three snapshots. Another validation test for our numerical code is based on the simulation of the Newtonian fluid. For a pressure difference $\Delta P=7.857$ calculated between the radial position $r=6$ and the inflow boundary, at $r=3$, at time 10.55, the max v_r at $r=6$, obtained from the analytical solution presented by Middleman (1977), is $v_{r,\max}=0.944$. Exactly the same value is predicted by our code at that position.

The effect of a relatively small fluid yield stress on the main characteristics of the flow can be seen in Fig. 15. This figure presents the same two variables as Fig. 14, but for $\mathrm{Bn}=0.5$, and $N=400$ at two time instants. The yield stress increases the fluid resistance to flow and requires a higher inlet pressure $P_{\mathrm{in}}=19.86$ to reach the same initial dimension-

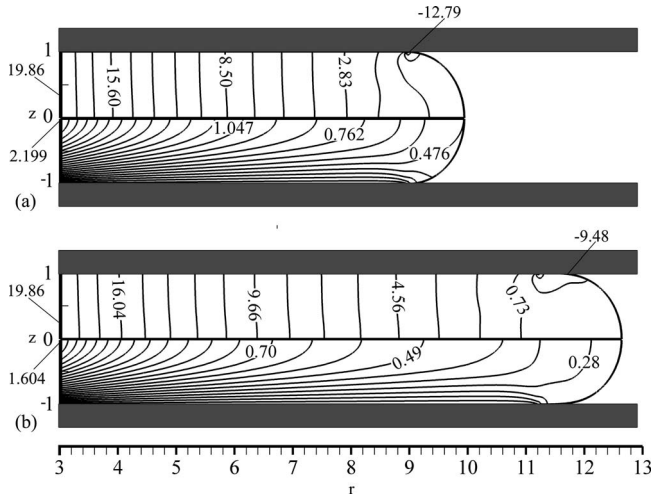

FIG. 15. Contours of the pressure field, upper half, and the radial velocity component, lower half, of a viscoplastic material between two parallel disks at (a) $t=3.03$ and (b) $t=10.84$ for $(\mathrm{Ca},\mathrm{Bn},l_1,l_2,P_{\mathrm{in}})=(10^3,0.5,400,3,5,19.86)$. The number of contour lines for both variables in each of the two snapshots is 24. The M1 mesh was used.

less velocity, while keeping the rest of the parameters the same with those in the previous simulation. It is clear that the contours of pressure are not straight here, as for a Newtonian fluid (compare with Fig. 14), but vary slightly in the axial direction, even far from the triple contact point. As for v_r, its contours in Fig. 15 resemble those for the Newtonian fluid. There are of course quantitative differences between the two cases. In the two snapshots, the tip of the interface has reached the positions $r=9.929$ and 12.629, respectively. The tip of the Newtonian fluid, in each of the first two snapshots of Fig. 14, has reached radial positions of $r=9.959$ and 12.736. Even though the Newtonian fluid extended radially at longer distances, its v_r decreased less from its initial value at the tip, than it did for the viscoplastic material, to 48.8% against 47.6% for the viscoplastic and to 30.2% against 26.8%, indicating that the latter decelerates faster.

We have seen in the case of pipe flow that higher values of the yield stress affect qualitatively the wetting of the tube wall by the fluid. A question that arises is whether this effect takes place also in the case of radial flow between parallel disks. Figure 16 shows the flow field at three different time instants for a viscoplastic fluid with $\mathrm{Bn}=5$ and $N=400$, which under the same values of the remaining parameters requires a much higher pressure $P_{\mathrm{in}}=53.13$ at the inflow boundary. At very early times, first the free surface deforms and then the triple contact point starts moving from its initial position at $r_c=8$. At time $t=0.49$ [see Fig. 16(a)], it is at $r_c=8.06$. Thereafter, the contact point remains stationary and part of the interface starts to develop parallel to the disk wall without the fluid coming into contact with it. The mechanism is the same as in the pipe flow: after the initial front deformation that requires intense fluid flow near it, during which the stress remains above the yield value, the front does not deform appreciably which—coupled with the shear-free condition on it—leads to stress lower than the yield value resulting in unyielded material there. The same figure also illustrates the contours of v_z in its upper half and of constant v_r in its lower half. The axial velocity varies mainly in the region near the triple contact point and the free surface of the fluid. In the first snapshot, we observe that the maximum value of the axial velocity, which is equal to 0.147, is near the free surface and below the triple contact point, since the fluid there moves toward the

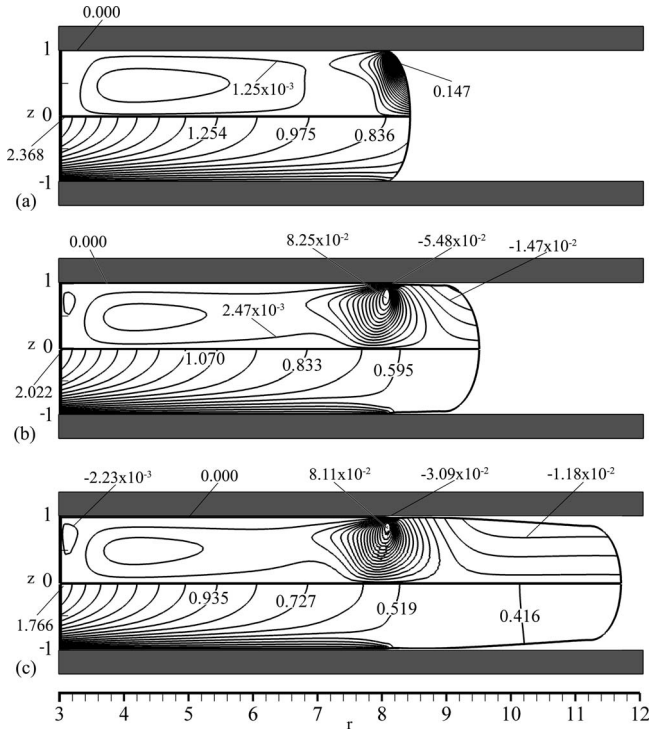

FIG. 16. Contours of the axial, upper half, and the radial, lower half, velocity component of a viscoplastic material between two parallel disks at (a) $t=0.49$, (b) $t=2.32$, and (c) $t=7.28$ for $(\mathrm{Ca},\mathrm{Bn},N,l_1,l_2,P_{\mathrm{in}})=(10^3,5,400,3,5,53.13)$. There are 25 contour lines for v_z and 18 for v_r in each one of the three snapshots.

wall as the interface becomes deformed. Subsequently, the max v_z value decreases significantly with time, becoming 8.25×10^{-2} at time $t=2.32$ and 8.11×10^{-2} at time $t=7.28$, at a location still close to the triple contact point. Moreover, after the fluid has detached from the wall [see Figs. 16(b) and 16(c)], the velocity field changes significantly. Near the triple contact point, it rearranges due to the transition from the no-slip condition to a shear-free flow. Ahead of it, the axial velocity takes negative values indicating that the material is very slowly moving away from the wall. Further downstream, v_z still takes negative values of the same order of magnitude with the previous ones, which result in the increasing distance between the fluid and the disk surface. This is caused by mass conservation, which requires that the radial expansion of the detached fluid is accompanied by an axial contraction. In addition, we observe that v_z assumes small values near the inflow boundary. One would expect 1D flow to occur in this region and, therefore, the axial velocity to be zero. This effect is most probably due to the condition that is applied on the pressure at the inflow boundary. As it can be readily shown from the momentum balance for this kind of flow, the pressure depends strongly on the radial and weakly on the axial direction (see also Fig. 18). Unfortunately, it is not possible to derive an analytical solution for the pressure without involving the (misleading) lubrication approximation for this kind of flow and, therefore, we have chosen to impose weakly the mean value of the pressure all along the inflow boundary, as described in Sec. II. We expect that the flow field very close to the inflow boundary will be slightly affected by this condition, causing this small variation in the axial velocity. However, this should not have a significant effect on the flow away from the entrance and in the region

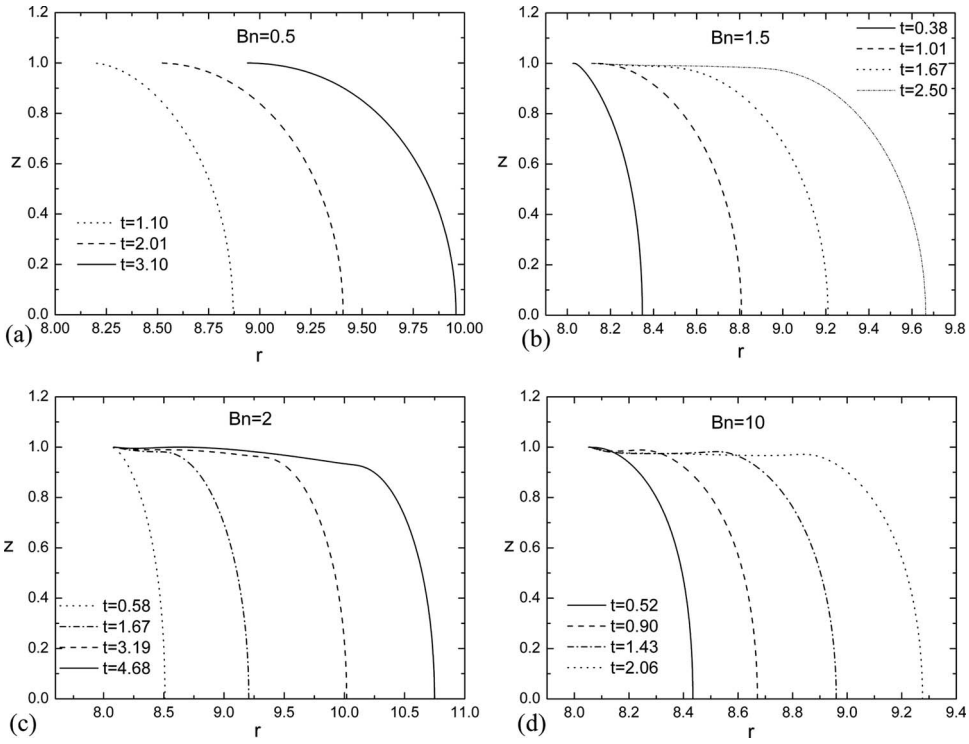

FIG. 17. Time evolution of the shape of the fluid/air interface for a viscoplastic material with (a) Bn=0.5, (b) Bn=1.5, (c) Bn=2, and (d) Bn=10.

of the free surface, which is of primary importance in this work. This is also supported by the fact that even though the pressure takes its mean value all along the inflow boundary, its 2D character is restored very close to it. The variation of v_r resembles the one for the Newtonian case in the region defined between the triple contact point and the inflow boundary. Because of the radial expansion of the material, mass conservation enforces a decrease in the radial velocity, which however, remains much larger than the axial component throughout the material. Ahead of the contact line, the radial velocity drastically changes its spatial variation and decreases in the radial direction only, approaching the variation of v_r in a shear-free extensional flow.

The effect of viscoplasticity can be seen more clearly by examining the development of the free surface for various Bn, as presented in Fig. 17. For a material with rather low values of Bn [Fig. 17(a)], the contact line moves as time passes, while the interface deforms and its shape turns from a semi-parabolic profile at early times into a semi-circular one at later times, resembling the limiting case of a Newtonian fluid. Increasing the value of the Bingham number to Bn=1.5, the Newtonian-like shape of the interface is lost at large times, since the contact line remains stationary and the interface deforms significantly. At time $t=2.50$, part of the free surface becomes almost parallel to the disk surface. The transition from this part of the free surface to its curved front remains very smooth and rounded. Increasing further the Bingham number to Bn=2 increases the departure of the flattened part of the interface from the wall as it attains a negative slope at long times. A common feature of the interfaces for intermediate and large Bingham numbers is that just ahead of the triple contact point, they bent downward, a pattern

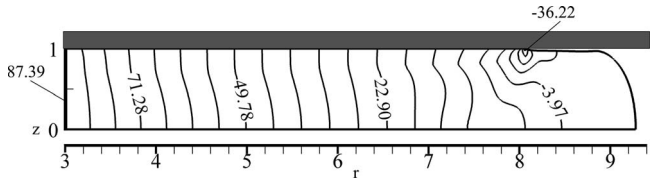

FIG. 18. Contours of the pressure field of a viscoplastic material with Bn=10 between two parallel disks at $t=2.06$. The rest of the dimensionless parameters are $(\mathrm{Ca}, N, l_1, l_2, P_{\mathrm{in}})=(10^3, 400, 3, 5, 87.39)$. The number of contour lines shown is 24. The M1 mesh was used.

which is retained for all the time instants. Moving further ahead in the radial direction, the upper flattened part of the interface rises again toward the disk surface and this becomes more significant at larger times. The decreased velocity gradients give the material behind the curved part of the front an increased effective viscosity as time passes. As a result, it becomes more difficult for the material to advance in its primary (radial) direction and easier to move axially toward the disks, where the stress singularity at the contact point still generates a smaller viscosity there. At time $t=4.68$, this part of the interface came very close to the disk surface and at the next time step, when an air-envelop was created, we decided to stop our simulation. In order to further investigate this behavior of the viscoplastic materials, we decided to perform a series of simulations in the range $0.5 \leq \mathrm{Bn} \leq 5$, which are not presented here for conciseness and we found out that the more viscoplastic the material, the longer it takes the envelope of air to form and the larger it gets. Even further ahead from the triple contact point, the interface turns more sharply away from the wall to join with the curved part of the front. A similar behavior is observed for the viscoplastic material with Bn=5. Increasing further the dimensionless yield stress to Bn=10, the interface of the material also diverges from the wall. Its shape presents another qualitative change: its part along the wall is nearly straight and such an envelope of air is not created. The mechanism leading to wall detachment is the same as for the flow in a pipe: when the front assumes a pseudo-steady shape, $\|\underline{\underline{\tau}}\|$ decreases, increasing the local viscosity. Then, the fluid momentum in a fountain-type flow is not enough to bring the fluid in contact to the wall. The different front shapes are generated here by two effects of the increasing Bn: the viscosity at the curved front increases faster, almost "freezing" its shape earlier when it is closer to the wall, so that it extends to its larger radial distance, as for Bn=10. Alternatively, the velocity decreases slower, allowing it to continuously deform and extend radially while decreasing axially, by mass conservation, as for Bn=2.

We have seen that the pressure in the Newtonian case changes in the radial direction only away from the front (see Fig. 14) and how this picture changes for a viscoplastic material with Bn=0.5. A further increase in the yield stress changes the pressure field drastically. Figure 18 illustrates the contour lines of pressure at time $t=2.06$ for the case of a viscoplastic material with Bn=10 and $N=400$, which requires $P_{\mathrm{in}}=87.39$ under the same values of the remaining parameters as in the Newtonian case. This plot demonstrates a more intense dependence of pressure on the axial coordinate. Each contour line near the mid-plane is shifted radially in the direction of the flow, while its remaining part turns away from the front. Again, the maximum values of pressure arise at the inflow boundary and, then, in the rest of the domain it decreases toward its minimum (negative) values at the contact point, where the contour lines are highly distorted due to the singularity that arises there.

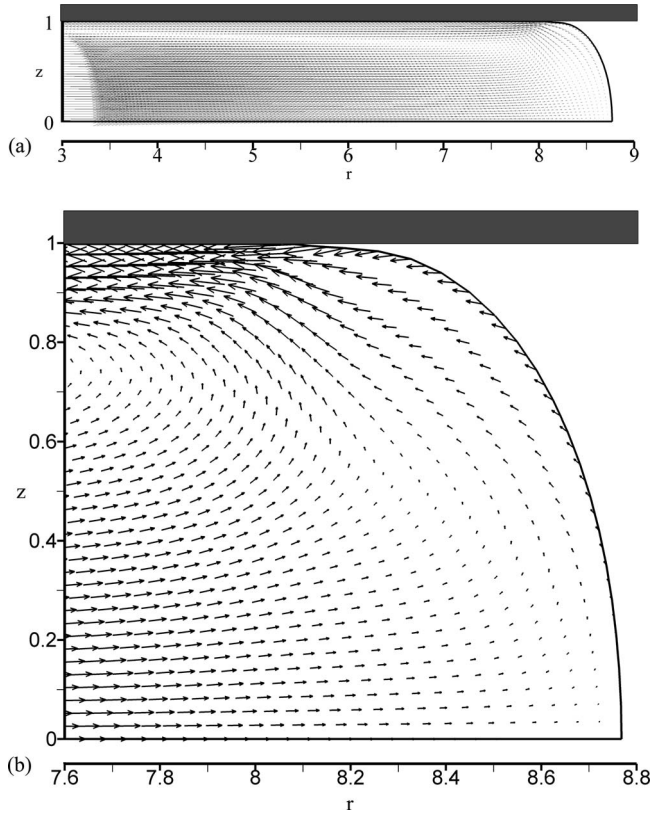

FIG. 19. Vectors of the velocity for a viscoplastic material with Bn=5, relative to the tip velocity. (a) The entire domain where the area of minimum velocity is shown and (b) a close-up in the region of the triple contact point.

A clearer picture of radial injection can be obtained by examining the velocity field from the point of view of an observer moving with the tip of the flow front. The resulting velocity vectors are presented in Fig. 19(a). This snapshot was taken at time $t=1.00$, shortly after the fluid detaches from the disk, for a viscoplastic material with Bn=5. A close-up of this figure for a region near the triple contact point is presented in Fig. 19(b). We observe that a line is formed extending from the inflow boundary to a little behind the radial position of the triple contact point, where the velocity as a vector attains a minimum. This line is close to, but it is not parallel to the wall, as it is in axial fountain flow. The reason for this departure is that in contrast to the pipe flow, the radial flow between the disks never reaches a fully developed profile, even near the inflow boundary, because the material elements encounter an ever-increasing cross section as they advance radially. Thus, a fluid element that lies close to the wall and the inflow boundary has the same velocity with a fluid element, which is located at a lower axial position and downstream. Now, we return to what the observer at the front tip sees. The fluid elements that reside at the mid-plane remain there because of their zero v_z and decelerate as they approach the tip where their velocity is zero by definition. The fluid elements between the line of minimum velocity and the mid-plane move toward the interface, while the ones above this line move toward the inflow boundary. Proceeding along the front from the tip to the contact point we can see, successively, that the vectors first turn toward the wall being vertical to the mid-plane, then they turn backward becoming parallel to the plane of

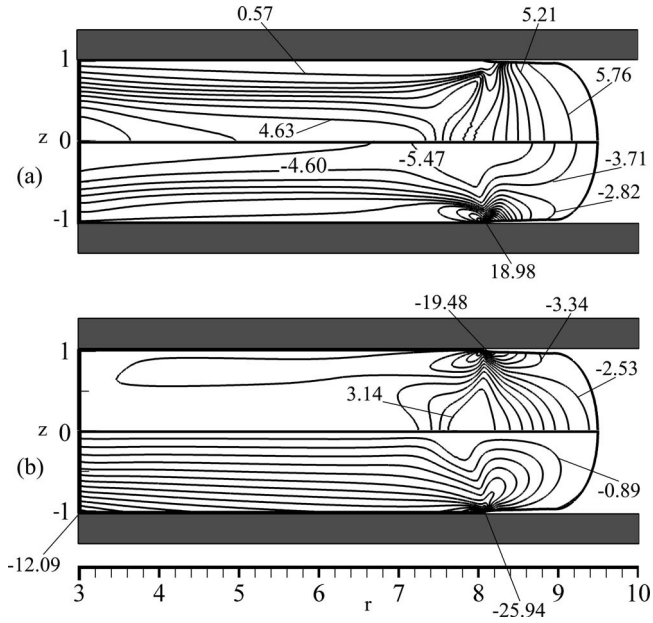

FIG. 20. Stresses of a viscoplastic material with Bn=5 between parallel disks. (a) Circumferential $\tau_{\theta\theta}$ upper half and radial τ_{rr} lower half. (b) Axial τ_{zz} upper half and the shear stress τ_{rz} lower half. The rest of the dimensionless parameters are $(\mathrm{Ca}, N, l_1, l_2, P_{\mathrm{in}}) = (10^3, 400, 3, 5, 53.13)$. The number of contour lines is 12 for $\tau_{\theta\theta}$ and 30 for each one of the other components of the stress tensor.

symmetry at some point near the rounded edge of the free surface, and finally even closer to the contact line they are inclined and slightly point away from the wall. The weaker and more uniform flow exists closer to the mid-plane and the liquid front. Due to the deceleration of the flow, the second invariant of the rate of strain decreases with time, which means that the effective viscosity increases locally. As the material flows radially and rises near the interface to contact the disk, its momentum is not sufficient for it to contact the wall causing in this way its detachment from it.

Interestingly, our prediction of material detachment from the wall is in agreement with the experimental observations by Bates and Bridgwater (2000). They conducted experiments with radial flow of pastes maintaining a constant flow rate. In order to monitor the position of the interface with respect to the disk surface and the force exerted by the disk on the fluid, they used flow visualization techniques and pressure transducers, respectively. They showed that as the paste flows radially outward, the contact of the material with the wall is lost. This is in fact what we predict with our simulations. They further attempted to explain this behavior of the fluid based on the relative magnitude and the direction of the normal stresses that they measured in the interface region. They argued that the radial stress τ_{rr} takes negative values, while the circumferential one $\tau_{\theta\theta}$ takes larger and positive values. As a result, the axial stresses τ_{zz} has to take negative values, forcing the interface to diverge from the wall. Since these authors did not give the data needed to calculate our dimensionless parameters, we can only compare our predicted stresses in terms of their order of magnitude and sign. Figure 20 illustrates the stress components we calculate at time $t=2.32$ for the case of a viscoplastic material with Bn $=5$. In Fig. 20(a), the contours of $\tau_{\theta\theta}$ and τ_{rr} are depicted in the upper and lower half of the domain, respectively, while in Fig. 20(b) the contours of τ_{zz} and τ_{rz} are given in the upper and lower half, respectively. After the triple contact point, which lies at the radial

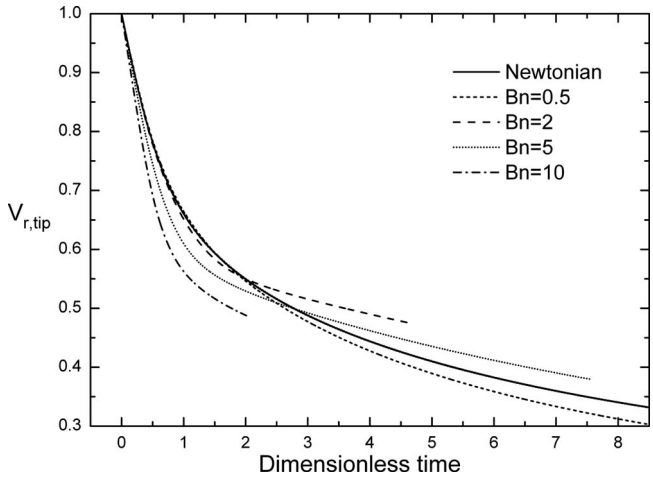

FIG. 21. Time evolution of the radial component of the velocity at the interface tip $V_{r,\mathrm{tip}}$ for various Bn. The rest of the dimensionless parameters are $(\mathrm{Ca}, l_1, l_2)=(10^3, 3, 5)$.

position 8.06, and toward the free surface, the circumferential stresses take positive values up to 5.89. In the same area, typical values for the radial normal stresses reach -3.71, while indeed, the axial normal stresses take much larger but negative values -19.48, concurring with the observations reported by these two researchers. The highest value of shear stress is located on the contact line, and around it, its contours are highly distorted. Moving away from the interface and toward the entrance, all isolines tend to become straight and with a small slope with respect to the disk surface. This weakly 2D character of the stress even near the inflow boundary derives mainly from the dependence of the radial component of the velocity on both spatial coordinates.

In order to examine the effect of Bn on the time evolution of the radial velocity of the flow front tip in more detail, we plotted in Fig. 21 its radial velocity $V_{r,\mathrm{tip}}$ versus the dimensionless time. We observe that at times smaller than $t=1.90$, as the Bn number increases the curve of the tip velocity falls more abruptly toward the horizontal axis. Hence, the higher the degree of viscoplasticity is, the more intense the deceleration of the fluid becomes in this time interval. This happens because the externally applied pressure has to overcome the increase of the effective viscosity, as the velocity gradients decrease due to the deceleration of the flow, more so the higher the yield stress. However, at longer times, the curves of the velocity tip corresponding to Bn=2 and Bn=5 are above the curve of Bn=0.5 and even the Newtonian one. This is caused by the fact that, for the first two cases, detachment of the material from the disk wall occurs. Thus, the shear forces exerted by the disk remain constant and this results in a smaller deceleration of the two viscoplastic materials. Moreover, between these two cases, the one with larger Bingham number (Bn=5) flows slower than the other one (Bn=2). In the case of flow inside a pipe, discussed in Sec. IV A, the flow rate becomes constant for large values of the Bingham number after a certain time. Clearly, this is not the case for the radial flow between parallel disks. As the fluid advances the front moves to larger radial positions and, therefore, the same volume of fluid has to go through a larger cross section, resulting in the significant decrease in the mean velocity. Indeed, these results are in qualitative agreement with findings by Peysson (private communication, 2006), who performed experiments using Bentonite mud with varying yield stress levels. We should note here that the simulation for Bn=2 was stopped prematurely at time $t=4.68$ to avoid the formation

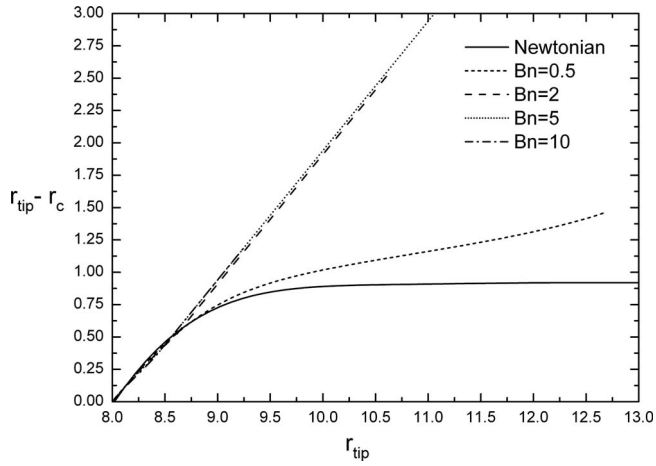

FIG. 22. Variation in the radial distance between the flow front tip and the triple contact point r_{tip}-r_c, with the radial position of the front tip r_{tip} for various Bn numbers between two parallel disks.

of the air inclusion between the material and the disk, mentioned earlier, which cannot be accommodated without major changes in the current software and was not pursued. On the other hand, the curves with Bn=5 and Bn=10 also terminate sooner than the Newtonian case or the one for Bn=0.5, but for a totally different reason, which will be made clear below.

It would be interesting to examine how the radial distance between the flow front tip and the triple contact point r_{tip}-r_c depends on the radial position of the front tip r_{tip} for various Bn numbers. As we can see in Fig. 22, the difference of these two positions initially increases for a Newtonian fluid but eventually levels out as the free surface tends to assume a cross section of constant shape, just as in the case of pipe flow. From the simulation, we found that r_{tip}-r_c tends to the value of 0.919 in comparison to the corresponding value of 0.830 in the case of pipe flow. For material with low viscoplasticity (Bn=0.5), the initial variation of r_{tip}-r_c is close to the one for a Newtonian fluid. However, its value seems to be increasing monotonically as the fluid-air interface advances without tending to a limiting value, at least for in the time interval that the simulation was performed. Increasing the Bn number further, we observe that because of the detachment of the fluid from the disk walls, r_{tip}-r_c increases linearly with r_{tip} at a larger slope.

Again the same important questions must be examined in this geometry also: does a critical Bn exists for detachment and does the fluid stop moving at a particular radial distance? As in pipe injection, we performed three sets of simulations keeping in each one $\overline{\text{Bn}}$ constant, i.e., keeping the same pressure drop for the same material. We then increased/decreased the initial amount of fluid that exists between the disks from the inflow boundary at $l_1=3$ up to $l_1+l_2 \equiv r_{c,\text{init}}$, which is the initial radial position of the contact point. The results are presented in Fig. 23, which presents the detachment length $r_{c,\text{det}}$, as a function of the initial length $r_{c,\text{init}}$. Clearly, the behavior similar to that in pipe flow, e.g., for $\overline{\text{Bn}}=0.042$ all three points fall on the same line, which has a smaller slope than the $y=x$ line. As the Bn increases, the radial distance that the fluid covers before it is detached from the disk wall increases. Consequently, all viscoplastic fluids will detach from the disks and those with higher Bn will detach earlier. Furthermore, increasing $\overline{\text{Bn}}$, the corresponding line approaches the line $y=x$ and its slope tends to unity, which is not surprising, because the material becomes more viscoplastic and is detached almost im-

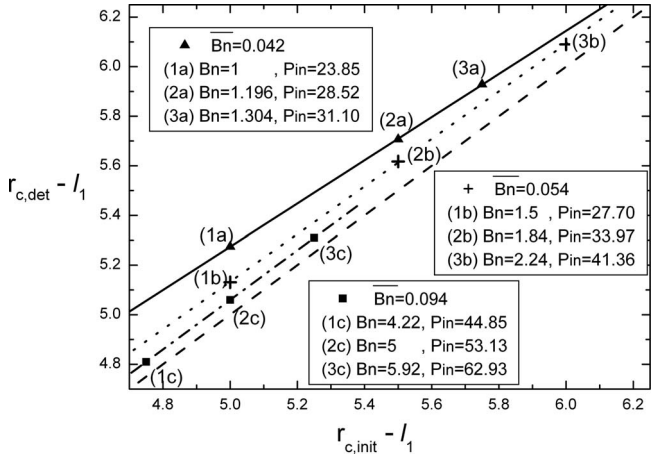

FIG. 23. Dependence of the location of the triple contact point at detachment on its initial radial position for three sets of Bn numbers, each corresponding to a single $\overline{\text{Bn}}$, for fluid injection between parallel disks. The slope of the line with $\overline{\text{Bn}}=0.042$ is 0.871, the slope for $\overline{\text{Bn}}=0.054$ is 0.959, and that for $\overline{\text{Bn}}=0.094$ is 0.999.

mediately from the wall. One could expect the line with slope almost unity ($\overline{\text{Bn}}=0.094$) to coincide with the $y=x$ line. Instead, it is slightly offset upward. This is caused by the initial intense rearrangement of the material near the front and the contact point, which allows a small translation of the contact point. As far as the question for the stopping length is concerned because the radial flow between parallel disks is always decelerating, a finite stopping length should exist. However, its precise determination is not possible with the Papanastasiou model as explained below.

As we have already seen in Fig. 16, the values of both velocities, radial and axial, have rather small values and gradients near the front, and they continuously decrease with time. As a result, the stresses that the fluid experiences in that area may decrease significantly as time passes. In order to examine whether unyielded material arises in the flow domain, we need to examine the contour lines of the second invariant of the stress tensor. These are presented in Fig. 24 for Bn=5 at time $t=7.28$. For clarity, we have plotted some contours of $\|\underline{\underline{\tau}}\|$ only in the range (5.05,5.07). Clearly, the values of $\|\underline{\underline{\tau}}\|$ decrease in the radial direction, while at the tip they have their minimum value $\approx 101\%$ of the Bn. In the next time instant, the flow will decelerate further and the value of $\|\underline{\underline{\tau}}\|$ at the tip will get closer or even become equal to the Bn, indicating that unyielded material arises there. Therefore, after this instant the material should stop moving. The material with Bn=10 behaves similarly. As explained earlier, however, according to the Papanastasiou model, even then finite motion of the material at that point is allowed, albeit with very large

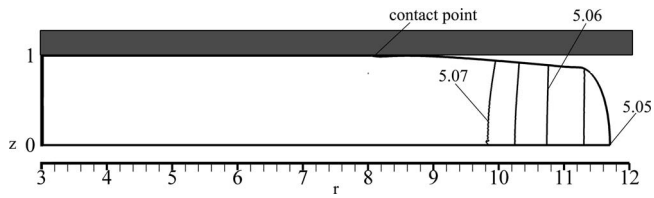

FIG. 24. Contours of the second invariant of the stress tensor of a viscoplastic material with Bn=5. The rest of the dimensionless parameters are $(\text{Ca}, N, l_1, l_2, P_{\text{in}})=(10^3, 400, 3, 5, 53.13)$.

viscosity and this is due to the fact that the condition for the yield surface given by $\|\tau\| = \mathrm{Bn}$ is not equivalent to $\dot{\gamma}=0$. Indeed, the rate of deformation at the tip is small and very slow radial flow still exists even there. According to Bates and Bridgwater (2000), who conducted experiments for radial flow of viscoplastic materials at constant flow rates, cracks appear at the external edge of the material. This could possibly be attributed to the fact that the flow of the yielded material is obstructed by the surrounding unyielded regions leading to those cracks. Considering that all these additional physical effects require including three dimensional flow and material deformation, we decided to terminate the simulations just before unyielded material could arise at the front tip.

V. CONCLUDING REMARKS

We examined the transient injection flow of a viscoplastic material inside a pipe or in the space between two parallel and coaxial disks. The material is driven by a constant pressure drop. The transient simulations allow us to determine for each problem (a) the velocity and pressure fields, (b) the domains of the unyielded material, and (c) the shape and the location of the liquid-air interfaces, at each time instant. All the calculations were performed using the mixed finite element/Galerkin method coupled with a quasi-elliptic mesh generation scheme for describing the large deformations of the physical domain. This scheme was combined with a mesh reconstruction procedure and a local mesh refinement technique to produce an improved discretization near the free surface and to accelerate the computations without losing the desired accuracy.

Results from a complete parametric analysis have been presented. We examined mainly the effect of the yield stress on the basic characteristics of the two flows. In the pipe flow for a Newtonian fluid, there is complete agreement with previous experimental data. At low Bn numbers, the flow is decelerating resembling the one for a Newtonian fluid, while the contact point translates to very long distances, before detachment should occur. Unyielded material arises only in the core region and expands both radially and axially with time. Material detaches from the tube wall more readily for highly viscoplastic fluids. For these materials, the liquid/air interface is extended with time and develops a segment nearly parallel to the wall. The wetting of the tube in this case stops and the triple contact point does not move, while the flow assumes a steady flow rate and a pressure distribution that does not change significantly with time. The higher the Bn number is, the earlier the detachment occurs, and, therefore, the higher the velocity that the material attains. Unyielded material arises in the core region of the tube and behind its front. However, the former does not expand at all because the flow now is not decelerating, while the latter grows significantly in the axial direction with time. Apparently, detachment should take place even for arrangements with low Bn, but after the flow has decelerated considerably, hence, the flow is not expected to stop in any case.

Wall detachment also occurs in the radial flow of a viscoplastic material between two parallel disks. In this case, the flow remains decelerating despite the wall detachment because of the increase of the cross section through which a fluid element advances. The materials which detach from the wall of the disks start to move faster than a less viscoplastic material, which does not detach from the wall, or even than the Newtonian fluid, after certain time instants. Wall detachment was observed experimentally by Bates and Bridgwater (2000) in radial flow of a paste between two parallel disks. The air/liquid interface of a viscoplastic material deviates even more from the Newtonian one as Bn increases. As the material is extended radially outward, the free surface moves parallel to the disk wall, and there an envelope of air may be created. The more viscoplastic the material is, the longer it takes for such an envelope to form and the greater it gets.

References

Barnes, H. A., "The yield stress—A review or '$\pi\alpha\nu\tau\alpha\rho\epsilon\iota$'—everything flows?," J. Non-Newtonian Fluid Mech. **81**, 133–178 (1999).

Bates, A. J. D., and J. Bridgwater, "The radial flow of pastes and gels," Chem. Eng. Sci. **55**, 3003–3012 (2000).

Behrens, R. A., M. J. Crochet, C. D. Denson, and A. B. Metzner, "Transient free-surface flows: Motion of a fluid advancing in a tube," AIChE J. **33**(7), 1178–1186 (1987).

Berger, J. L., and C. G. Gogos, "A numerical simulation of the cavity filling process with PVC in injection molding," Polym. Eng. Sci. **13**(2), 102–112 (1973).

Beris, A. N., J. A. Tsamopoulos, R. C. Armstrong, and R. A. Brown, "Creeping motion of a sphere through a Bingham plastic," J. Fluid Mech. **158**, 219–244 (1985).

Billingham, J., and J. W. J. Ferguson, "Laminar unidirectional flow of thixotropic fluid in a circular pipe," J. Non-Newtonian Fluid Mech. **47**, 21–55 (1993).

Bingham, E. C., *Fluidity and Plasticity* (McGraw-Hill, New York, 1922).

Bird, R. B., W. E. Stewart, and E. N. Lightfoot, *Transport Phenomena* (Wiley, New York, 1960).

Bogaerds, A. C. B., M. A. Hulsen, G. W. M. Peters, and F. P. T. Baaijens, "Stability analysis of injection molding flows," J. Rheol. **48**(4), 765–785 (2004).

Burgos, G. R., A. N. Alexandrou, and N. M. Entov, "On the determination of yield surfaces in Herschel-Bulkley fluids," J. Rheol. **43**(3), 463–483 (1999).

Chatzidai, N., A. Giannousakis, Y. Dimakopoulos, and J. Tsamopoulos, "On the elliptic mesh generation in domains containing multiple inclusions and undergoing large deformations," J. Comput. Phys. **228**, 1980–2011 (2009).

Chatzimina, M., C. Xenophontos, G. C. Georgiou, I. Argyropaidas, and E. Mitsoulis, "Cessation of annular Poiseuille flows of Bingham plastics," J. Non-Newtonian Fluid Mech. **142**, 135–142 (2007).

Chung, D. H., and T. H. Kwon, "Numerical studies of fiber suspensions in an axisymmetric radial diverging flow: The effects of modeling and numerical assumptions," J. Non-Newtonian Fluid Mech. **107**, 67–96 (2002).

Co, A., and W. E. Stewart, "Viscoelastic flow from a tube into a radial slit," AIChE J. **28**(4), 644–655 (1982).

Coyle, D. J., J. W. Blake, and C. W. Macoslo, "The kinematics of fountain flow in mold-filling," AIChE J. **33**(7), 1168–1176 (1987).

Dai, G., and B. R. Bird, "Radial flow of a Bingham fluid between two fixed circular disks," J. Non-Newtonian Fluid Mech. **8**, 349–355 (1981).

Davis, A. M. J., and T.-Z. Mai, "Steady pressure-driven non-Newtonian flow in a partially filled pipe," J. Non-Newtonian Fluid Mech. **41**, 81–100 (1991).

Dimakopoulos, Y., and J. A. Tsamopoulos, "Transient displacement of a viscoplastic fluid by air in straight or suddenly constricted tubes," J. Non-Newtonian Fluid Mech. **112**, 43–75 (2003a).

Dimakopoulos, Y., and J. A. Tsamopoulos, "A quasi-elliptic transformation for moving boundary problems with large anisotropic deformations," J. Comput. Phys. **192**, 494–522 (2003b).

Dimakopoulos, Y., and J. A. Tsamopoulos, "Transient displacement of Newtonian and viscoplastic liquids by air in complex tubes," J. Non-Newtonian Fluid Mech. **142**(1–3), 162–182 (2007).

Dubash, N., and I. A. Frigaard, "Conditions for static bubbles in viscoplastic fluids," Phys. Fluids **16**(12), 4319–4330 (2004).

Florides, G. C., A. N. Alexandrou, and G. C. Georgiou, "Flow development in compression of a finite amount of a Bingham plastic," J. Non-Newtonian Fluid Mech. **143**, 38–47 (2007).

Frigaard, I. A., S. Leimgruber, and O. Scherzer, "Variational methods and maximal residual wall layers," J. Fluid Mech. **483**, 37–65 (2003).

Frigaard, I. A., and C. Nouar, "On the usage of viscosity regularization methods for visco-plastic fluid flow computation," J. Non-Newtonian Fluid Mech. **127**, 1–26 (2005).

Grillet, A. M., A. C. B. Bogaerds, G. W. M. Peters, F. P. T. Baaijens, and M. Bulters, "Numerical analysis of flow surface defects in injection molding flow," J. Rheol. **46**(3), 651–669 (2002).

Huang, X., and D. R. Oliver, "Processing properties of ceramic paste in radial flow," Br. Ceram. Trans. **98**(1), 1–5 (1999).

Karapetsas, G., and J. A. Tsamopoulos, "Transient squeeze flow of viscoplastic materials," J. Non-Newtonian Fluid Mech. **133**, 35–56 (2006).

Lipscomb, G. G., and M. M. Denn, "Flow of Bingham fluids in complex geometries," J. Non-Newtonian Fluid Mech. **14**, 337–346 (1984).

Matsoukas, A., and E. Mitsoulis, "Geometry effects in squeeze flow of Bingham plastics," J. Non-Newtonian Fluid Mech. **109**(2–3), 231–240 (2003).

Mavridis, H., A. N. Hrymak, and J. Vlachopoulos, "Deformation and orientation of fluid elements behind an advancing fluid front," J. Rheol. **30**(3), 555–563 (1986).

Mavridis, H., A. N. Hrymak, and J. Vlachopoulos, "Transient free-surface flows in injection mold filling," AIChE J. **34**(3), 403–410 (1988).

Middleman, S., *Fundamentals of Polymer Processing* (McGraw-Hill, New York, 1977).

Mills, K. W., "Observation of horizontal subsidence movement at Baal Bone Colliery," *The Proceedings of the 5th Triennial Conference on Coal Mine Subsidence: Current Practice Issues* (Society of the Institution of Engineers, Australia, 2001), pp. 26–28.

Papanastasiou, T. C., "Flows of materials with yield," J. Rheol. **31**, 385–404 (1987).

Papanastasiou, T. C., N. Malamataris, and K. Ellwood, "A new outflow boundary condition," Int. J. Numer. Methods Fluids **14**, 587–608 (1992).

Peysson, Y., B. Herzhaft, M. Mainguy, and E. Lecolier, "Methode et dispositif de mesure du seuil d'écoulement et de la viscosite a faible gradient de cisaillement d'un fluide complexe," Patent No. FR2864237 A1 (2005).

Poslinski, A., and J. A. Tsamopoulos, "Nonisothermal parison inflation in blow molding," AIChE J. **36**(12), 1837–1850 (1990).

Poslinski, A., and J. A. Tsamopoulos, "Inflation dynamics of fluid annular menisci inside a mold cavity. I. Deformation driven by small gas pressure," Chem. Eng. Sci. **46**(1), 215–232 (1991).

Roquet, N., and P. Saramito, "An adaptive finite element method for Bingham fluid flows around a cylinder," Comput. Methods Appl. Mech. **192**, 3317–3341 (2003).

Rose, W., "Fluid-fluid interfaces in steady motion," Nature (London) **191**(4785), 242–243 (1961).

Saad, Y., *Iterative methods for sparse linear systems*, 2nd ed. (SIAM, New York, 2000).

Schenk, O., and K. Gärtner, "Solving unsymmetric sparse systems of linear equations with PARDISO," FGCS, Future Gener. Comput. Syst. **20**(3), 475–487 (2004).

Schenk, O., K. Gärtner, and W. Fichtner, "Scalable parallel sparse factorization with left-right looking strategy on shared memory multiprocessor," BIT **40**(1), 158–176 (2000).

Smyrnaios, D. N., and J. A. Tsamopoulos, "Squeeze flow of Bingham plastics," J. Non-Newtonian Fluid Mech. **100**, 165–190 (2001).

Szabo, B., and I. Babuska, *Finite Element Analysis* (Wiley, New York, 1991).

Tsamopoulos, J. A., M. F. Chen, and A. V. Borkar, "On the spin coating of viscoplastic fluids," Rheol. Acta **35**, 597–615 (1996).

Tsamopoulos, J. A., Y. Dimakopoulos, N. Chatzidai, G. Karapetsas, and M. Pavlidis, "Steady bubble rise in Newtonian and viscoplastic fluids and conditions for bubble entrapment," J. Fluid Mech. **601**, 123–164 (2008).

Tsiveriotis, K., and R. A. Brown, "Solution of free-boundary problems using finite-element/Newton methods and locally refined grids: Application to analysis of solidification microstructure," Int. J. Numer. Methods Fluids **16**, 827–843 (1993).

Vinay, G., A. Wachs, and J.-F. Agassant, "Numerical simulation of weakly compressible Bingham flows: The restart of pipeline flows of waxy crude oils," J. Non-Newtonian Fluid Mech. **136**, 93–105 (2006).

Wu, P. C., C. F. Huang, and C. G. Gogos, "Simulation of the mold-filling process," Polym. Eng. Sci. **14**(3), 223–230 (1974).